Directional flank spreading at Mount Cameroon volcano: Evidence from analogue modeling

M. Kervyn, Benjamin van Wyk de Vries, T.R. Walter, M.S. Njome, C.E. Suh, G. Ernst

AGU PUBLICATIONS

JGR

Journal of Geophysical Research: Solid Earth

RESEARCH ARTICLE
10.1002/2014JB011330

Special Section:
Stress, Strain and Mass Changes at Volcanoes

Key Points:
- Mount Cameroon morphology provides evidence of gravitational deformation
- Dynamics of the deformation is analyzed through analogue models
- Directional flank spreading over nonuniform weak sediments controls deformation

Supporting Information:
- Readme
- Figure S1
- Figure S2

Correspondence to:
M. Kervyn,
makervyn@vub.ac.be

Citation:
Kervyn, M., B. van Wyk de Vries, T. R. Walter, M. S. Njome, C. E. Suh, and G. G. J. Ernst (2014), Directional flank spreading at Mount Cameroon volcano: Evidence from analogue modeling, *J. Geophys. Res. Solid Earth*, *119*, 7542–7563, doi:10.1002/2014JB011330.

Received 28 MAY 2014
Accepted 22 SEP 2014
Accepted article online 26 SEP 2014
Published online 27 OCT 2014

Directional flank spreading at Mount Cameroon volcano: Evidence from analogue modeling

M. Kervyn[1], B. van Wyk de Vries[2], T. R. Walter[3], M. S. Njome[4], C. E. Suh[4], and G. G. J. Ernst[5]

[1]Department of Geography, Earth System Science, Vrije Universiteit Brussel, Brussels, Belgium, [2]Laboratoire Magma et Volcans, Université Blaise Pascal, Clermont-Ferrand, France, [3]GFZ German Research Center for Geosciences, Potsdam, Germany, [4]Department of Geology and Environmental Science, University of Buea, Buea, Cameroon, [5]Department of Geology and Soil Science, Ghent University, Gent, Belgium

Abstract Mount Cameroon is characterized by an elongated summit plateau, steep flanks, and topographic terraces around its base. Although some of these features can be accounted for by intrusion-induced deformation, we here focus on the contribution of edifice-scale gravitational spreading in the structure of Mount Cameroon. We review the existing geological and geophysical data and morphostructural features of Mount Cameroon and surrounding sedimentary basins. Volcanic ridge gravitational spreading is then simulated by scaled analogue models on which fault formation is recorded using digital image correlation. Three sets of models are presented (i) models recorded in cross section (Type I), (ii) models recorded from above with a uniform (Type IIa), and (iii) nonuniform ductile layer (Type IIb). Type I models illustrate the formation of faults accommodating summit subsidence and lower flank spreading. Type IIa models favor displacement perpendicular to the long axis, with formation of a summit graben and basal folds, but fail to reproduce the steep flanks. Type IIb models investigate the effect of spatial variations in sediment thickness and/or properties consistent with geological evidence. Directional spreading of the volcano's central part perpendicular to the long axis is accounted for by a sediment layer with restricted lateral extent and increasing thickness away from the volcano axis. The later model closely reproduces key features observed at Mount Cameroon: steep upper flanks are accounted for by enhanced lateral spreading of the lower flanks relative to the summit. The relevance of these findings for understanding flank instabilities at large oceanic volcanoes is finally highlighted.

1. Introduction

High volcanoes are inherently unstable piles of poorly consolidated material, affected by deformation processes that contribute to limit the maximum height they can reach [e.g., *Delaney*, 1992; *Borgia et al*., 2000; *Grosse et al*., 2009]. Repetitive magmatic intrusions along volcanic rift zones and gravitational spreading are recognized as the two main processes controlling internal structure and flank deformation at large volcanoes [*Le Corvec and Walter*, 2009 and references therein], as documented at oceanic islands, e.g., Kilauea (Hawaii, USA) [e.g., *Morgan et al*., 2003] or Piton de la Fournaise (Reunion Island) [*Oehler et al*., 2005], large continental volcanoes, e.g., Etna (Sicily, Italy) [e.g., *Borgia et al*., 1992], and Martian shields [e.g., *McGovern and Morgan*, 2009; *Platz et al*., 2011; *Byrne et al*., 2013, 2014]. In these studies, flank movements are thought to be facilitated by ductile layers below (i.e., marine or deltaic sediments) or within the volcanic edifice (i.e., hydrothermally altered rocks).

Le Corvec and Walter [2009] investigated the structures and deformation induced by magmatic intrusions along a volcanic rift zone and by gravitational spreading in a volcanic ridge, and the strong coupling between these two processes, using analogue models. They simulated the deformation of a half topographic ridge between two glass panes: this setting was required to simulate magmatic intrusion along a rift zone but prevented faults' propagation from one flank of the ridge to the other below the summit. They illustrated that both processes are associated with flank deformation, but with contrasted structural features, and that their relative influences on the structural evolution of a volcano are difficult to differentiate. Flank gravitational spreading is accommodated by an outward dipping listric fault, not always reaching the ridge summit, and associated antithetic faults. Rift zone intrusions induce summit graben subsidence and the coherent outward displacement of the flank along a subhorizontal decollement layer: this deformation was accompanied by localized steepening of the flank and shallow instability or thrusts and folds at the flank base, depending on the depth of the intrusion [*Le Corvec and Walter*, 2009].

In-depth understanding of deformation processes is essential for the interpretation of geophysical data, the assessment of risks associated with slope instabilities or to constrain the interactions between volcano structures and magmatic systems. Building on the results of *Le Corvec and Walter* [2009], we here focus on the deformation dynamics and structures induced by gravitational spreading, using Mount Cameroon as an illustrative test case.

Mount Cameroon volcano is a 4095 m high lava-dominated volcano built over weak sediments [*Suh et al*., 2001, 2003, 2008]. With a volume of ~1300 km^3, it is one of the most voluminous continental volcanoes together with Kilimanjaro (Tanzania) and Etna (Italy). Mount Cameroon's morphology displays a broad and flat summit plateau, ~30° steep upper flanks, sharp slope breaks, and gently sloping terraces around its base [*Gèze*, 1943; *Déruelle et al*., 1987]. A number of deformation processes [*Dzurisin*, 2007] are expected to take place at Mount Cameroon: magmatic deformation was interpreted from interferometric synthetic aperture radar data for the 1999 and 2000 eruptions [*Walter and Amelung*, 2003]; tectonic faulting is consistent with the elongation of Mount Cameroon along the Cameroon fracture line [*Déruelle et al*., 1987]; and gravity-driven mass movements was suggested by *Mathieu et al*. [2011] based on field investigation. This later study proposed a model in which the long flanks of Mount Cameroon are laterally spreading and its summit is subsiding, as evidenced by thrusts and folds observed in underlying Miocene sediments.

Yet this conceptual model of volcano spreading, or the one of magmatic intrusion presented by *Le Corvec and Walter* [2009], are unable to fully account for the observed steep upper flanks, for local slope instabilities or for the asymmetric distribution of thrust faults around the volcano. The continental and active tectonic setting of Mount Cameroon is ideal to document the edifice-scale deformation structures, to investigate processes responsible for unusually steep slopes (i.e., $>20°$) at other lava-dominated volcanoes [e.g., *Rowland and Garbeil*, 2000], and to unravel the potential influence of active tectonic structures on volcano deformation.

Building upon *Le Corvec and Walter* [2009] and *Mathieu et al*. [2011], the objective of this contribution is to investigate the deformation dynamics at Mount Cameroon and, specifically, to assess the contribution of gravitational spreading to the current volcano morphology, including the steep unstable upper slopes. We first review in details the geological setting and the volcano structure and morphology, as they provide essential constraints for the analogue models. Then we present new analogue experiments that simulate the gravitational spreading of a sand ridge over a ductile silicone layer. Models recorded in cross section (Type I) and from above (Type II) with varying ductile layer geometries are presented and analyzed with an image correlation technique. We thereafter discuss if the dynamics of gravitational spreading is consistent with the morphology observed at Mount Cameroon and consider the contribution of magmatic intrusions to the overall deformation dynamics.

2. Geological Setting

Mount Cameroon is the largest volcano within the Cameroon Volcanic Line (Figure 1a), a ~2000 km long alignment of Cenozoic alkaline intraplate volcanoes extending from the oceanic crust of the Gulf of Guinea to the Adamawa Plateau in Tchad (Figure 1). The origin of the Cameroon Volcanic Line remains a matter of debate [e.g., *Déruelle et al*., 2007; *Reusch et al*., 2010; *Gallacher and Bastow*, 2012; *Milelli et al*., 2012].

Seismic and gravity studies of the Cameroon Volcanic Line suggest that magmatism in the Miocene induced an asymmetric uplift of the oceanic crust by as much as 3 km [*Meyers and Rosendahl*, 1991; *Meyers et al*., 1998], and a ~1 km amplitude uplift in the continental sector of the Cameroon Volcanic Line, centered on the Adamawa plateau [e.g., *Meyers and Rosendahl*, 1991; *Poudjom Djomani et al*., 1997]. *Reusch et al*. [2010] showed this uplift to be associated with a linear low seismic velocity zone in the upper mantle. Hence, a crustal uplift, associated with reduced sediment deposition and/or increased erosion can also be expected below Mount Cameroon, further enhanced by uplift caused by magma intrusions at the onset of volcano growth [*Mathieu and van Wyk de Vries*, 2009].

Mount Cameroon is located at the transition between oceanic crust and continental crust and overlies sedimentary basins (see below). With seven confirmed eruptions in the twentieth century [e.g., *Fitton et al*., 1983; *Suh et al*., 2003; *Bonne et al*., 2008; *Njome et al*., 2008; *Suh et al*., 2008; *Wantim et al*., 2011, 2013], Mount Cameroon is the most active volcano of the Cameroon Volcanic Line. It is dominantly made up of overlapping lava flows of alkaline basalt composition, with a lesser but probably significant proportion of pyroclastic

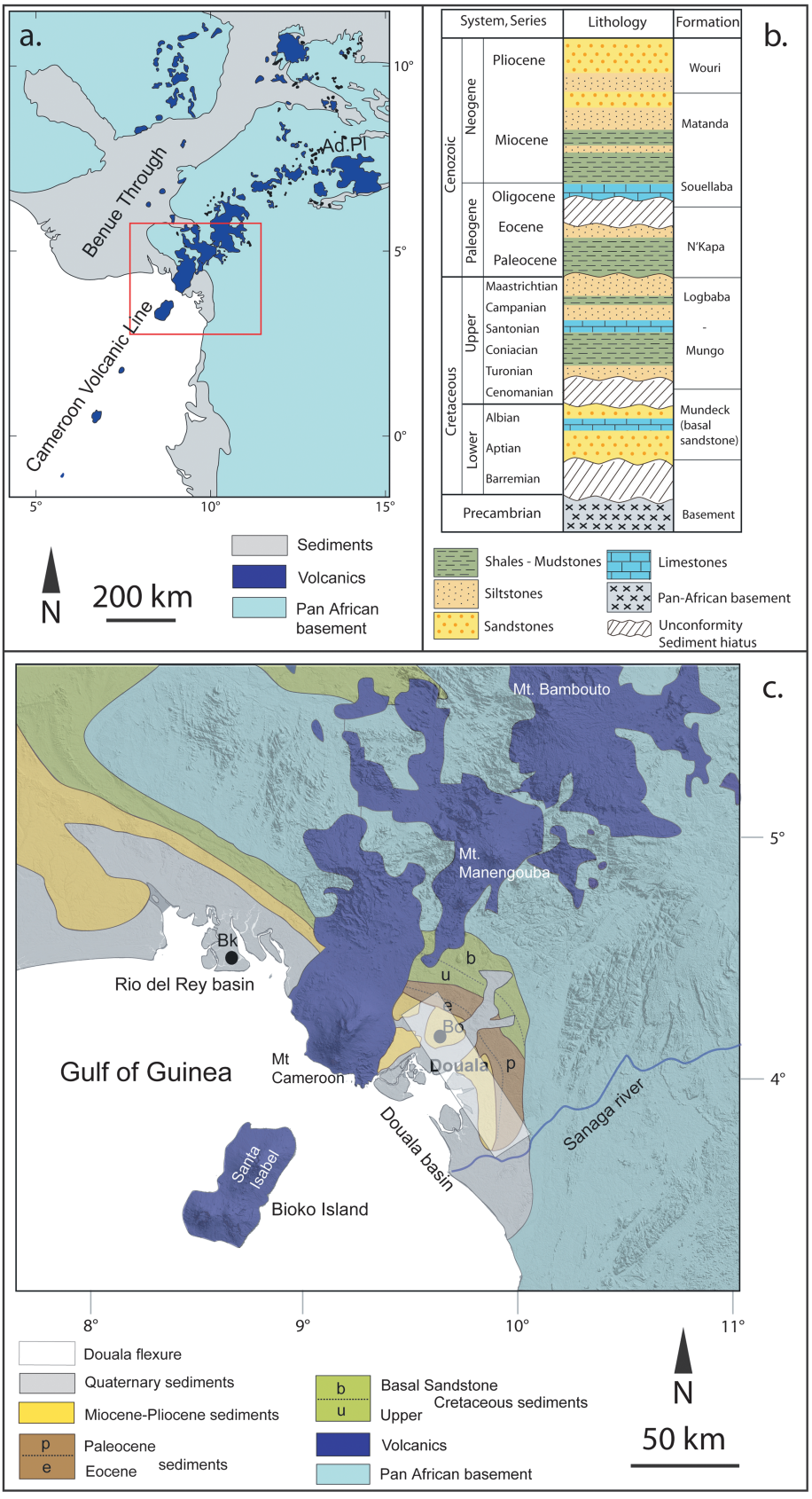

Figure 1

cones and dyke intrusions along its central axis [*Mathieu et al*., 2011]. Volcano growth may have started 1–3 Ma ago [*Hedberg*, 1968; *Marzoli et al*., 2000; *Wandji et al*., 2009]. At its base, early stage lava flows of Mount Cameroon cover Miocene sediments which outcrop along topographic terraces (see below). Field evidence suggests that these sediments were uplifted and deformed relative to the surrounding sedimentary basins [*Hedberg*, 1968; *Meyers and Rosendahl*, 1991; *Mathieu et al*., 2011].

The structure, geometry, and composition of sedimentary basins underlying volcanoes can affect their structure and deformation [*Borgia et al*., 2000]; we therefore here describe the characteristics of the underlying sedimentary basins, with specific attention to weak sediment layers that can undergo ductile deformation under gravitational loading. Mount Cameroon is built upon thick sediments, which have deposited over Pan-African Mobile Belt crystalline and metamorphic rocks. To the east and NW of Mount Cameroon, the Douala and Rio del Rey sedimentary basins are observed, respectively. These basins are half grabens initiated during the Aptian-Albian (Figure 1c) [*Benkhelil et al*., 2002]. The two basins are bounded to the north by a set N120°E striking listric faults, which have accommodated seaward basin deepening [*Dumort*, 1968; *Reyre*, 1984; *Moreau et al*., 1987; *Benkhelil et al*., 2002].

The basins' stratigraphy encompasses Aptian to Pliocene fluvial and marine formations and Pleistocene delta sediments (Figures 1b and 1c). The Aptian-Albian *Mundeck Formation* is a 600 m thick coarse fluvial sandstone unit (i.e., basal sandstone, Figure 1b). The postrifting Upper Cretaceous *Mungo-Logbaba Formation* consists of marine siltstones with intercalated shallow limestones, marls, and shales (~500 m thick, Figure 1b) [*Regnoult*, 1986; *Ponsard and Saugy*, 1989; *Meyers et al*., 1996; *Brownfield and Charpentier*, 2006]. These Cretaceous sediments form a NW-SE trending outcrop located north of Mount Cameroon. More recent sediments gradually crop out further SW (Figure 1c).

In the Rio del Rey basin, Cretaceous sediments are unconformably overlain by Tertiary nonmarine sands, silts, and deltaic shales. In the Douala basin the Paleocene-Lower Eocene unit (*N'Kapa Formation*, >600 m thick, Figure 1b) consists of thick organic-rich shales, marls, and calcareous sandstones, whereas Oligocene to Miocene deposits (*Souellaba and Matanda Formations*, ~1000 m thick, Figure 1b) are mainly detritic gravels and sandstones with intercalated plastic clay beds [*Ponsard and Saugy*, 1989; *Brownfield and Charpentier*, 2006]. The post-Cretaceous stratigraphy does not correlate from the Douala to Rio del Rey basin across the Cameroon Volcanic Line.

In both basins, weak sediment layers have been documented. Several shale beds are characterized by abnormal pressure interpreted as undercompaction where shale was not able to expel its interstitial water after desmectisation [*Reyre*, 1984]. This interpretation is based on observations in the onshore wells of Bomono, East of Mount Cameroon, at ~2200 m depth toward the base of Lower Miocene deposits. Under high stress, these overpressured shales are highly mobile [*Reyre*, 1984]. This is consistent with diapiric rise of shales, deforming overlying Mio-Pliocene deposits, observed in Bakassi M1 well in the Rio del Rey basin [*Reyre*, 1984] (Figure 1c).

The depth to the Pan-African basement increases nonlinearly southward. The most significant increase in sediment thickness occurs along the *Douala flexure* directly north of Mount Cameroon, with depth-to-basement increasing from 1 to 3–4 km over a 20 km distance (Figure 1) [*Belmonte*, 1966]. The amount of water-rich ductile shale beds also increases dramatically south of the flexure. Sediment thickness in the Douala and Rio del Rey basin at the latitude of Mount Cameroon is estimated to vary from 3 to 5 km from NE to SW [*Ponsard and Saugy*, 1989].

The Rio del Rey and Douala basins may have been separated by prevolcanism regional uplift in the Miocene [*Meyers and Rosendahl*, 1991] so that a thinner sediment package is to be expected above the uplifted area. This is consistent with stratigraphic observations at the base of Mount Cameroon that

Figure 1. (a) Location of study area (red rectangle) and extent of the volcanics from the Cameroon Volcanic Line in West Africa (Ad.Pl.: Adamawa Plateau). (b) Generalized stratigraphic log of NW part of Douala sedimentary basin (adapted from *Regnoult* [1986], *Meyers et al*. [1996], and *Brownfield and Charpentier* [2006]). (c) Schematic geological map of Mount Cameroon and surrounding sedimentary basins, with shaded relief of the SRTM DEM in background (adapted from *Le Maréchal* [1975], *Chiarelli* [1976], *Regnoult* [1986], and *Brownfield and Charpentier* [2006]). The Douala flexure, characterized by a stepwise deepening of the sedimentary in the south-west direction is located by a white shading, according to *Belmonte* [1966]. Bk: Bakassi M1 well; Bo: Bomono well.

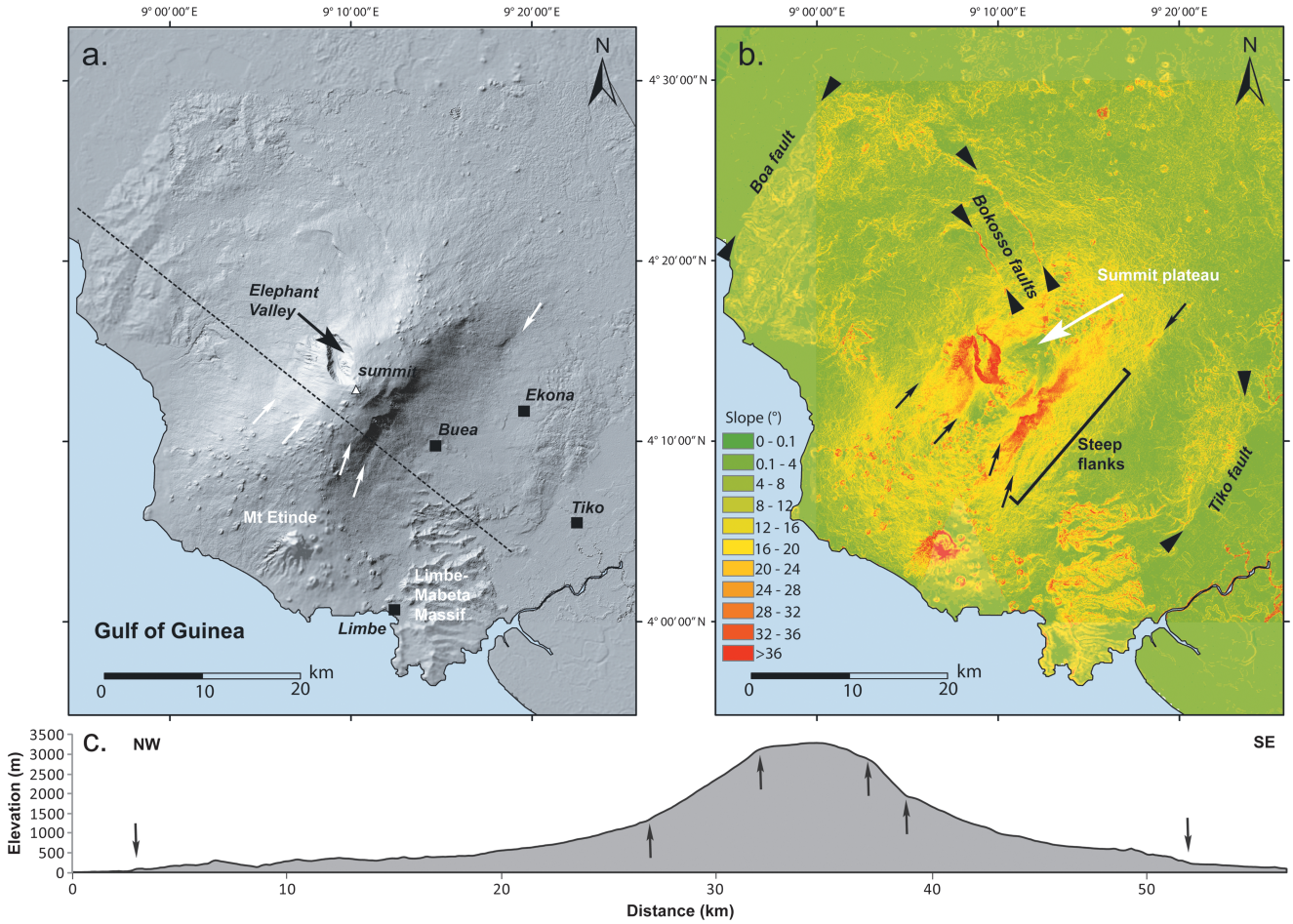

Figure 2. (a) Shaded relief (Sun azimuth: 315°N, elevation 45°) with location of main cities and (b) slope distribution of Mount Cameroon extracted from SRTM DEMs—combining the 1 and 3 arc second resolution—with indication of the main volcano-tectonic structures in between black triangles. (c) Representative topographic profile along stippled line shown in Figure 2a. Arrows point to sharp slope breaks.

indicate that Mount Cameroon's volcanic products intrude and overlie ~800 m of sedimentary deposits [*Dumort*, 1968; *Hedberg*, 1968; *Regnoult*, 1986].

In summary, Mount Cameroon is a large basaltic volcano built up over the last million years above a 3–5 km thick sequence of Cretaceous to Miocene mechanically weak sediments, characterized by mobile shale beds found at 2 to 4 km depth away from the Cameroon Volcanic Line axis. Type and thickness of sediments rapidly evolve from NE to SW. Crustal uplift and volcano growth reduced sediment deposition along the line axis and enhanced sediment accumulation off axis.

3. Volcano Morphology Analysis

Using the 30 m X-band Shuttle Radar Topography Mission-(SRTM) digital elevation model and comparing it with field data from *Mathieu et al*. [2011], we hereafter review the surface morphology (i.e., slopes, vent spatial distribution, fissures, or lineaments; Figures 2–4) and geology of MC in order to describe the structural map of this volcano. Together with the geological setting, this section provides constraints to assess the applicability of the analogue models to Mount Cameroon.

3.1. Terrain Slope

Mount Cameroon is a large volcano, elongated NE-SW, i.e., it has two long flanks, facing SE and NW, and two short flanks, facing NE and SW. It has a well defined volcanic rift zone marked by the alignment of eruptive

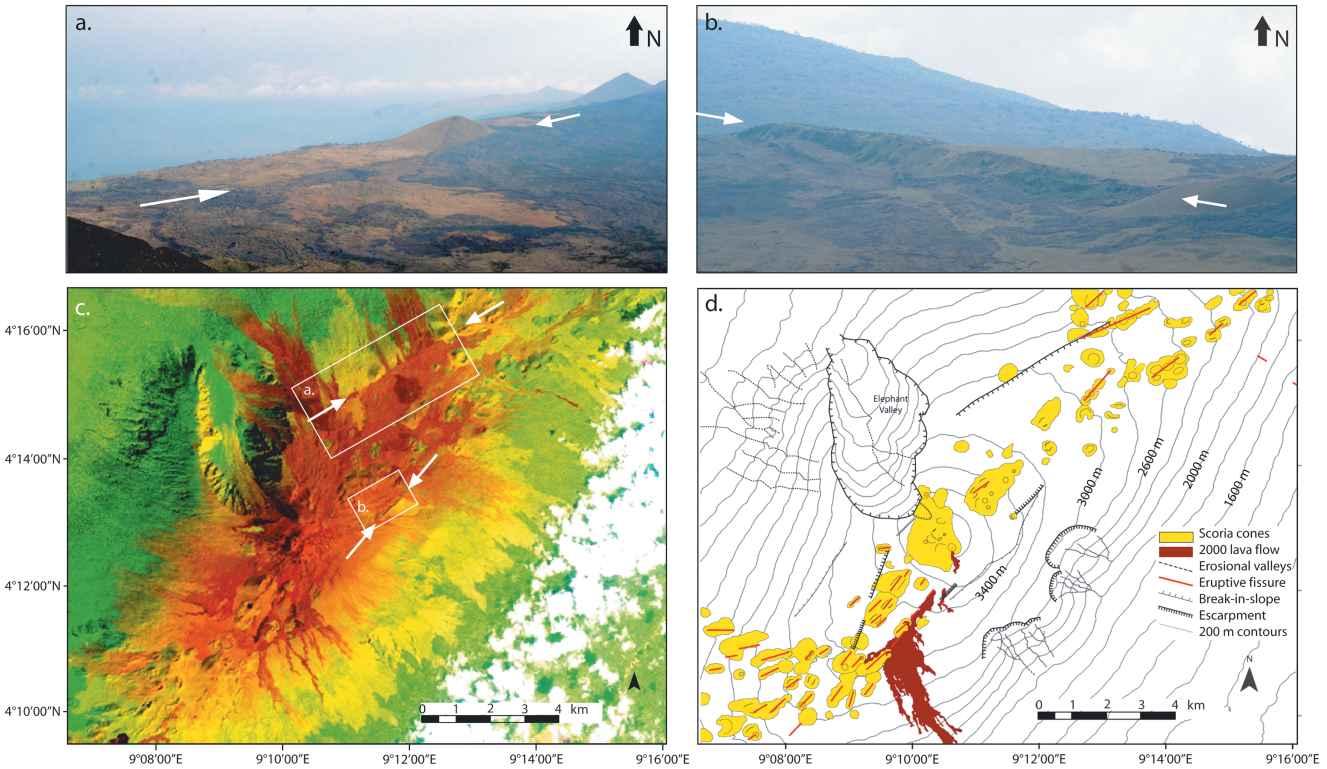

Figure 3. Field view looking (a) north and (b) NE from Mount Cameroon summit showing structures bordering a flat plateau (between white arrows); (c) Landsat ETM + of summit zone (acquired on 10 December 2000) showing structures affecting summit zone (white arrows); white rectangles mark the zones imaged in Figures 3a and 3b; (d) interpretative map with contour lines extracted from SRTM DEM (see Figure 2): the three outward facing escarpments on SE flanks are interpreted as landslide scars.

fissures and volcanic cones parallel to the elongation axis [*Tibaldi et al.*, 2013]. Mount Cameroon is characterized by terrains with contrasting slope gradients separated by sharp slope breaks (Figure 2).

The broad summit plateau is 5 × 12 km and has gentle slopes (<10°), except for some steep linear topographic steps (see below). Normal to the elongation axis, this gently sloping plateau turns abruptly into steeply sloping upper flanks (20–35°; Figure 2b). The upper part of the SE facing flank is linear and smooth, except for three subvertical scars attributed to landsliding (Figure 3). The base of the SE steep slope is marked locally by two sharp slope breaks (arrows in Figure 2) and a gradual transition to gently sloping lower flanks (<8°). The NW facing flank exhibits a broader and less linear upper flank characterized by moderate to steep slopes (15–30°). The central part of this flank is typified by a convex planar curvature, resulting in an outward bulge morphology dissected in its center by the 6 km long, 3.5 km wide, and <400 m deep Elephant Valley. The outer flank of this topographic bulge is the only zone of the upper flank to be clearly affected by a network of erosional gullies. Along the elongation axis, the volcano slopes are more irregular, depending on the density distribution of scattered pyroclastic cones, and remain on average <20° (Figure 2).

3.2. Distribution of Eruptive Vents

Eruptive vents correspond to sites of past eruption outbreaks at the surface and take the form of craters in pyroclastic cones and fissures. The eruptive fissures' orientation is inferred from the alignment of closely spaced vents, cone elongation, crater geometry, breaching direction, and from eruption accounts [*Tibaldi*, 1995; *Suh et al.*, 2003; *Njome et al.*, 2008; *Suh et al.*, 2011; *Wantim et al.*, 2011]. Across the summit plateau, most eruptive fissures are aligned along a N040°E direction, defining a narrow volcanic rift zone (Figure 3).

Vent concentrations (1.8–3.8 vent km^{-2}) are observed in broad zones centered at each extremity of the summit plateau (Figure 4a). Vent and fissure orientations are more scattered on the lower flanks, where pyroclastic cone concentration is <1 vent km^{-2} (Figures 4a and 4b). The NE part of the volcanic rift zone is characterized by two main vent alignments down to ~1200 m above sea level, oriented N015°E and N060°E,

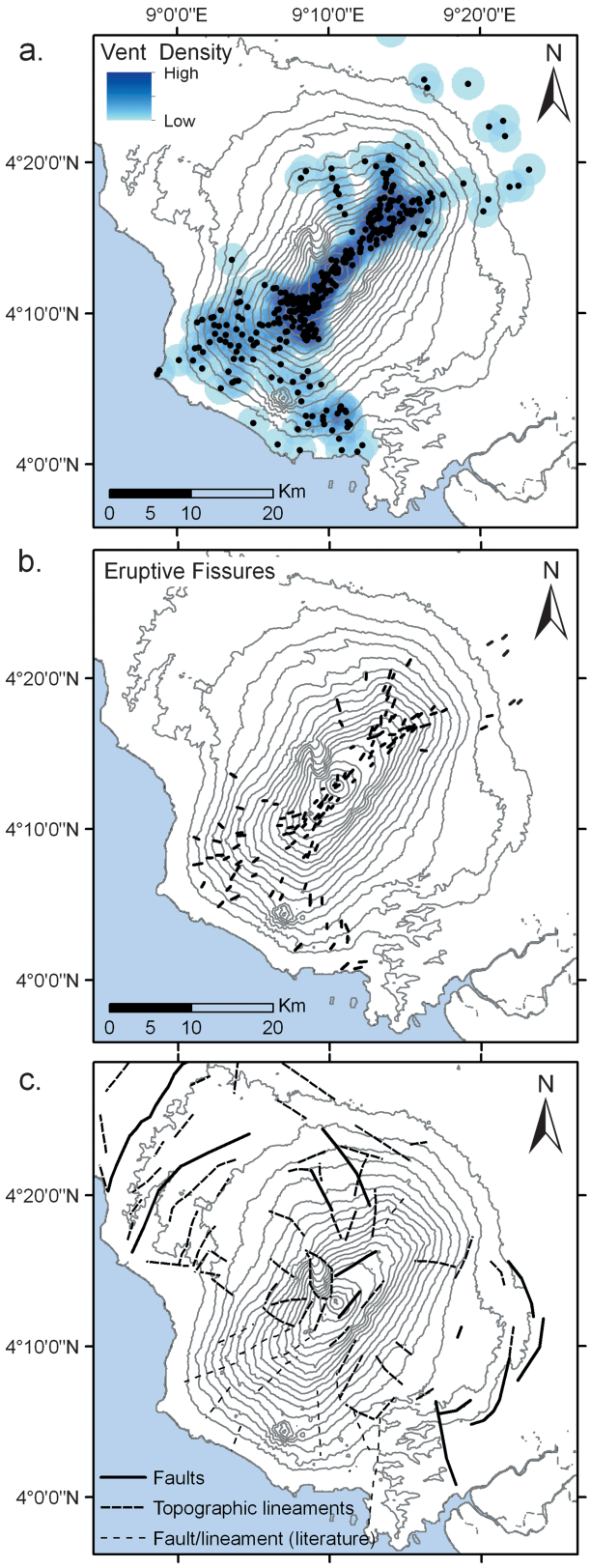

respectively. In the SW part of the volcanic rift zone, vents extend down to sea level in a broad zone, with eruptive fissures being mostly perpendicular to contour lines. No apparent vents are found on the steep flanks, except for vents and fissures aligned along the upward prolongation of the Bokosso faults on the NE flank (Figures 2–4).

3.3. Structural Lineaments

Structural lineaments are linear features characterized by a sharp topographic step and/or a lithological contrast. Several lineaments have previously been identified in the topography and some have associated seismicity (e.g., Bokosso faults; Figures 2 and 4) [*Déruelle et al.*, 1987; *Moreau et al.*, 1987; *Zogning*, 1988; *Ateba and Ntepe*, 1997; *Suh et al.*, 2001; *Suh et al.*, 2003; *Ateba et al.*, 2009].

Sharp topographic steps and steep slopes are observed at the base of Mount Cameroon and define ridges that are parallel to the volcano elongation axis. Northwest of the volcano, these ridges extend 30 km from the summit to the sharp topography of the N030°E trending Boa fault [*Zogning*, 1988] (Figure 2). These parallel ridges are 25–30 km long and are interpreted as thrust faults [e.g., *Mathieu et al.*, 2011].

These ridges are bordered laterally by structures subradial to Mount Cameroon, such as the well expressed and seismically active N330°E Bokosso faults on the north flank [*Ubangoh et al.*, 1997] (Figure 2). These lineaments can be traced back into Mount Cameroon's flanks and coincide with the edge of the steep upper flanks (Figures 2 and 5). Although the kinematics of these faults has yet to be characterized from seismic data, they are here interpreted as strike-slip to transtensional structures based on morphological interpretation.

Figure 4. Spatial distribution of volcanic vents and (a) vent density, (b) eruptive fissures, and (c) volcano-tectonic structures. Eruptive fissure orientations inferred from closely spaced vent alignment, crater, and cone elongation and cone breach direction. For volcano-tectonic structures, distinction is made between confirmed faults documented in previous studies, topographic lineaments, and other structures mentioned in literature but with limited or no topographic expression. Contour lines are every 200 m.

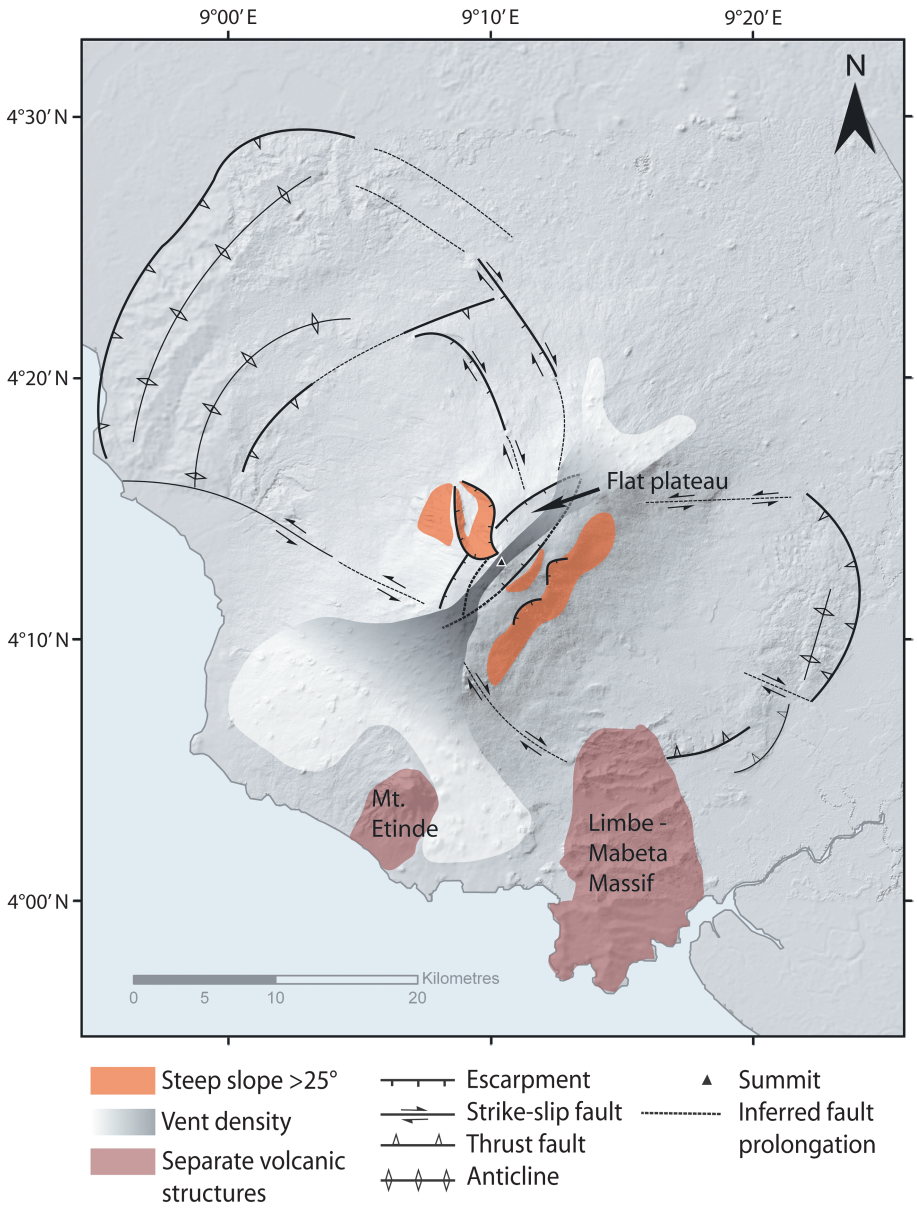

Figure 5. Conceptual interpretation of main structural elements for Mount Cameroon based on observations made in Figures 2–4. Structural lineaments are interpreted as thrust faults, strike-slip faults, or anticlines according to evidence from *Mathieu et al.* [2011] or results from analogue modeling presented in this study. Background image: shaded relief of SRTM DEM.

The SE base of the volcano is characterized by a flatter zone between Buea and Ekona which is rich in volcaniclastic deposits (Figure 2). This zone is bordered by a series of steep slopes, previously interpreted as the Tiko fault [*Zogning*, 1988]. The steep slopes actually define a 15 × 18 km lobe-shaped zone, elevated ~250 to 400 m above the surrounding sedimentary basin. The symmetry axis of this lobe is parallel but offset to the NE relative to the short axis of Mount Cameroon (Figure 5). The southern extent of this lobe feature coincides with the southern extent of the steep slopes on the SE flank (Figure 5). Field-based research recently showed that this SE lobe is made up of thrusted and folded Miocene sediments underlying Mount Cameroon lava flows [*Mathieu et al.*, 2011] and can therefore not be accounted by the sudden termination of volcanic lithologies.

The summit plateau of Mount Cameroon is also characterized by structural features (Figure 3). At the northern border of the summit plateau, a 6 km long structure striking N060°E cuts through pyroclastic cones and lava flows (Figure 3a). This structure is locally associated with 2–3 m of vertical offset, with downthrow of

the central plateau relative to the flanks. This structure is visible on the Landsat Enhanced Thematic Mapper Plus (ETM+) image as a buttress to the propagation of lava flows (Figure 3c); it is interpreted as an inward dipping normal fault. A second shorter structure (~1.5 km long) striking N047°E, with a greater vertical offset (10–15 m), is observed in the field to mark one of the main slope breaks on the east side of the summit plateau (Figure 3b). An extension of this structure is found close to the upper part of the main fissure of the 2000 eruption (Figure 3c). Preliminary radar interferometry analysis for the 1997–2001 period showed differential movement along this second structure during the last eruptive phase in 1999–2000 [*Walter and Amelung*, 2003]. This second structure, also interpreted as an inward dipping normal fault, is not located at the edge of the steep flank but delineates a secondary topographic step within the summit plateau (Figure 3).

Other structures were identified by previous workers [*Zogning*, 1988] within the lower rift zones; these have no topographic expression and are here interpreted as preferential eruptive fissure orientations (Figure 4c).

In summary, the morphostructural analysis allows the identification of the following main features (Figure 5): (1) an elongated volcanic ridge, (2) steeper across-axis than along-axis slopes, (3) a flat and fault-delimited summit plateau, (4) strike-slip faults on the midflank, most clearly expressed perpendicular to the volcano long axis (i.e., Bokosso faults), and (5) peripheral fold and thrust belts parallel to the long axis. The distribution of vents and summit structures is consistent with extensional stresses oriented perpendicular to the volcano elongation. We will show hereafter that this distribution is expected considering gravity-driven deformation of an elongated edifice [*Fiske and Jackson*, 1972; *Dieterich*, 1988; *Tibaldi et al*., 2013].

4. Methodology

4.1. Analogue Modeling Approach and Experimental Setup

In the following we test to which extent gravity-driven deformation contributes to structures and morphology of Mount Cameroon through analogue modeling experiments. The most dominant form of gravity-driven deformation occurring at many steep and highly elevated volcanoes is *volume-preserving spreading* [*Borgia et al*., 2000]. If the spreading thesis is consistent with the Mount Cameroon case, then similarities should be observed between analogue models and morphostructural features recorded for Mount Cameroon as summarized in Figure 5.

An experimental setup and analogue material similar to those in previous analogue modeling of gravitational deformation for volcanic cones are used [e.g., *Merle and Borgia*, 1996; *Walter et al*., 2006; *Delcamp et al*., 2008; *Platz et al*., 2011]. We use two types of setups (Types I and II), which both consist in a flat substratum made of horizontal ductile and brittle layers, which is overlain by an elongated cone or ridge (Figure 6). In the first setup (Type I), we place the model between two glass panes, 10 cm apart from each other (Figure 6a). A ridge, ~40 cm in width and ~11 cm high (Table 1), was rapidly built up above the horizontal layers. This setting, comparable to that used by *Le Corvec and Walter* [2009], enables the documentation of model deformation from the side and the identification of the dynamics for the main structures. One limitation is that the glass panes induce border effects, limiting motion of the analogue materials along the glass [*Schreurs et al*., 2006]. Because the observations are made along the glass, these are almost plane-strain experiments that provide a 2-D image of the deformation. In the second set-up (Type II), models were conducted in a 60×60 cm wooden box. A sand ridge, ~18×32 cm at the base and 4–5 cm in height, was rapidly emplaced above the horizontal substratum (Figure 6b). At the beginning of the experiments, the ridges are at their angle of repose (28°) and have a flat and linear summit crest.

The potentially ductile sediments underlying the volcano are simulated using a layer of polydimethylsiloxane (PDMS; Dow Corning SGM 36), a silicone Newtonian fluid of 4×10^4 Pa s viscosity. Natural white quartz sand ($<630\ \mu$m, median grain size Φ ~300 μm) mixed with 5 wt % of $<400\ \mu$m black sand is used as granular material to simulate both the brittle substratum and the volcano. Physical properties for the analogue materials are given in Table 1 and compared to corresponding values expected for Mount Cameroon.

The silicone PDMS layer was left overnight after emplacement to obtain a uniform thickness and to let air bubbles escape. The quasi-cohesionless sand was sifted to build up the brittle substratum and the ridge in order to obtain homogeneously densely packed sand as suggested by *Lohrmann et al*. [2003] or *Panien et al*. [2006].

A total of 26 Type I and 40 Type II models were analyzed. Two key parameters were systematically varied: the silicone layer thickness and its spatial extent. A silicone layer with uniform thickness in the range 0.5 to 4 cm,

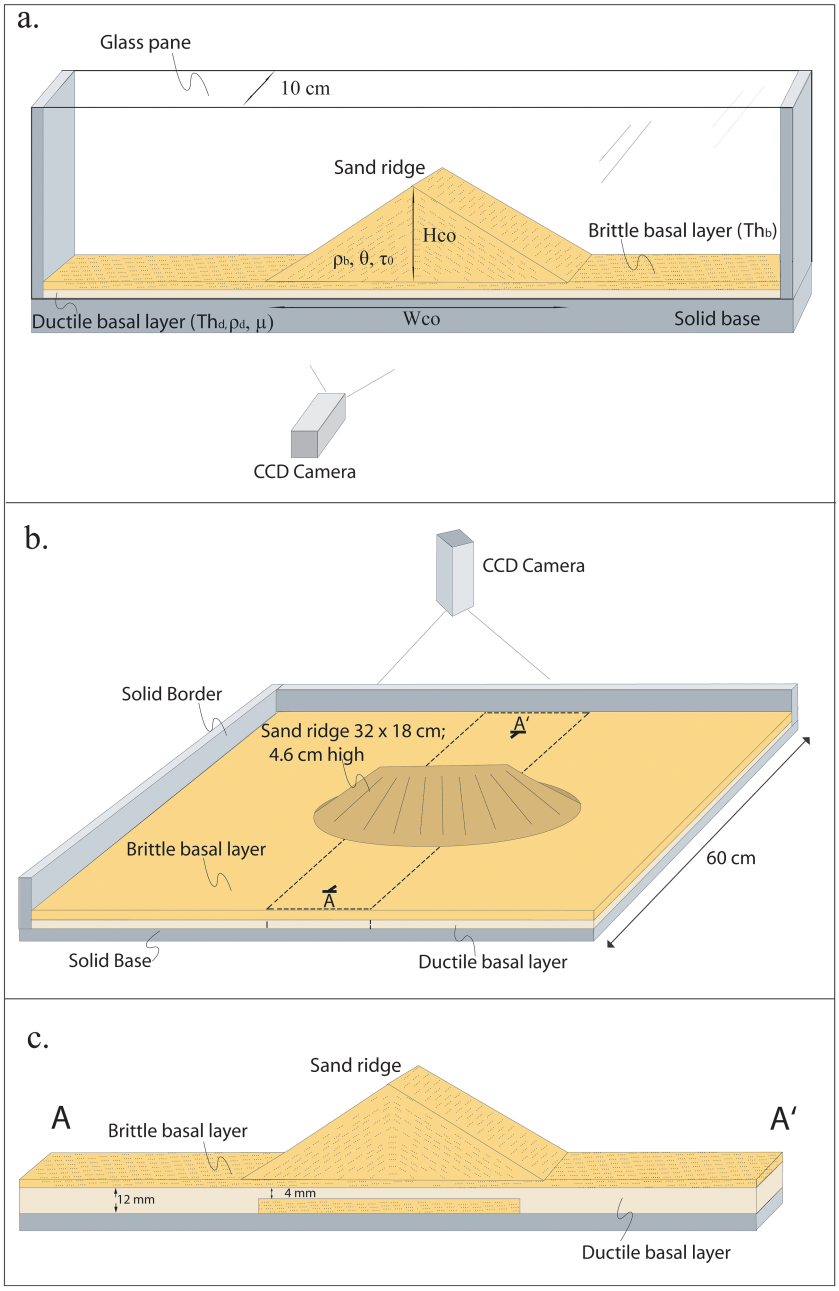

Figure 6. (a) Type I and (b) Type II analogue modeling experimental setups, with mention of dimensions, key geometrical, and physical parameters indicated; the extent of the silicone layer in Type IIb models is highlighted by the dashed line in Figure 6b. (c) Cross section along A-A′ line in Figure 6b illustrating the variation of silicone thickness in Type IIb model discussed in text (Figure 6c).

i.e., a silicone thickness/cone height (Th_d/H_{co}) of 0.05–0.4 for Type I and 0.1–1 for Type II models, was used to model the range of realistic natural conditions. Such a large range is needed due to the poor constraints on thickness or depth of the ductile sediments below Mount Cameroon. Increased silicone thickness simulates a higher sediment mobility, either due to greater thickness or lower viscosity in nature. The thickness of the brittle layer was also varied in the 0.5 to 2 cm range but was kept to a minimum for most experiments, as no or limited brittle rock overlies the Miocene sediments at Mount Cameroon.

Geological evidence available for the sedimentary basin indicates that significant variations in the total thickness and depth of ductile layers can be expected around Mount Cameroon. Whereas in Type I and Type

Table 1. Material Properties and Model-to-Nature Ratios for Analogue Modeling Applied to Mount Cameroon

Symbol	Parameters	Dimension (Unit)	Models	Nature	Model/Nature Ratio
H_{co}	Ridge Height	L (m)	$4–11 \times 10^{-2}$	4.1×10^{3}	$1–2 \times 10^{-5}$
W_{co}	Ridge Width	L (m)	$2–4 \times 10^{-1}$	$2.5–5 \times 10^{4}$	1×10^{-5}
Th_d	Ductile Layer Thickness	L (m)	$0.5–4 \times 10^{-2}$	$0.8–2 \times 10^{3}$	$1–2 \times 10^{-5}$
Th_b	Brittle Layer Thickness	L (m)	$0.5–2 \times 10^{-2}$	$0–5 \times 10^{2}$	$10^{-4}–10^{-5}$
ρ_d	Ductile Material Density	$M \cdot L^{-3}$ (kg/m^3)	970	2000–2500	0.38–0.48
ρ_b	Brittle Material Density	$M \cdot L^{-3}$ (kg/m^3)	1450	2500–2700	0.55–0.6
μ	Ductile Material Viscosity	$M \cdot L^{-1} \cdot T^{-1}$ (Pa s)	4×10^{4}	$10^{16}–10^{18}$	$10^{-12}–10^{-14}$
θ	Coefficient of friction		0.6	0.6	1
τ_0	Cohesion	$M \cdot L^{-1} \cdot T^{-2}$ (Pa)	<100	$10^{6}–10^{7}$	$10^{-4}–10^{-6}$
g	Gravity	$L \cdot T^{-2}$ (m s^{-2})	9.81	9.81	1
t	Time span of spreading	T (s)	3×10^{3}	$10^{12}–10^{13}$	$10^{-8}–10^{-9}$

IIa models, the ductile substratum is homogenous across the entire model, a third set of models (Type IIb) investigates the influence of a ductile layer of spatially variable thickness upon edifice deformation. Slope distribution and structural evidence at Mount Cameroon suggest that it is mostly the central part of the volcanic ridge that is deforming (Figure 5). The ridge was therefore emplaced orthogonally upon a long silicone band of limited width (i.e., 15 cm, half the ridge long axis, Figures 6b and 6c). The silicone layer was bordered by sand in order to obtain a flat surface with limited brittle material (i.e., <5 mm) over the silicone. Variable silicone band thicknesses were tested from $Th_d/H_{co} = 0.1$ to 0.5. Consistent with geological evidence, the thickness of the silicone was also varied along the silicone band. Type IIb experiment illustrated in results models the effect of an abrupt thickening of the silicone layer below the lower flanks, even though a more gradual, but so far unconstrained, transition may be expected in nature (Figure 6c). The ridge is built upon a 15 cm wide silicone band which is 0.4 cm thick below the central part of the ridge ($Th_d/H_{co} = 0.08$) and 1.2 cm thick below the lower flank and flat brittle layer ($Th_d/H_{co} = 0.24$).

Our experimental models focus exclusively on the effect of gravitational spreading on the deformation of a volcanic ridge. Deformation associated with magmatic intrusions or their influence on spreading structures was investigated in a separate set of experiments [see *Le Corvec and Walter*, 2009] and will be considered in the discussion of the results.

4.2. Scaling

In order to be comparable to natural volcanoes, analogue models need to be geometrically, kinematically and dynamically scaled. For scaling, we used the same approach developed in previous analogue modeling of volcano gravitational spreading [*Merle and Borgia*, 1996]. The different geometrical parameters are scaled with a model/nature ratio of 10^{-5}, i.e., 1 cm in analogue models represent 1 km in nature (Table 1).

The quartz sand used has an internal friction coefficient of 0.6, similar to natural brittle rocks. This ensures that fault geometry in analogue models will be comparable to fault geometry in natural volcanoes [*Schellart*, 2000]. The brittle material is generally assumed to nearly have a Mohr-Coulomb behavior [e.g., *Ramberg*, 1981]. In addition, *Lohrmann et al.* [2003] showed that ~300 μm quartz sand is characterized by strain-hardening and strain-softening effects similar to natural brittle rocks. The PDMS silicone has been used in many similar studies and was shown to be a relevant analogue for ductile natural rocks [*Schellart*, 2000].

Dynamic scaling is achieved if the gravitational stress ratio $\sigma^* = \rho^* \times g^* \times h^*$, where ρ^*, g^* and h^* are the model/nature ratios for density, gravitational acceleration, and height of the volcano, respectively. This calculation yields a stress ratio of $\sim 5 \times 10^{-6}$, indicating that the analogue volcano should be $\sim 5 \times 10^{6}$ times mechanically weaker than a volcano in nature. Low cohesion granular material is here used to simulate volcanoes with a bulk cohesion of up to 10^{7} Pa, the approximate cohesion of fresh nonfractured rock. The actual bulk cohesion of the volcano can be expected to be up to one order of magnitude lower as it is build up by lava flows fractured from cooling or from postemplacement deformation [*Hoek et al.*, 2002].

Kinematic scaling, i.e., the velocity at which the analogue model deforms relative to natural cases, is poorly constrained. Deformation velocities are entirely constrained by the balance between the brittle layer and volcano load, through its density and height, on the one hand, and the viscosity of the underlying material on the other [*Delcamp et al.*, 2008]. Natural viscosity values of ductile sediments are ill constrained and range

over several orders of magnitude. As the sand material is assumed to have a near Mohr-Coulomb behavior, kinematic scaling has no major effect on the structural architecture, the fault types, and their geometry. Thus, although the deformation velocity of analogue models cannot be directly compared with natural cases, our approach allows investigation of the structures associated with the deformation, which are controlled by the system geometry rather than by deformation velocity [*Delcamp et al*., 2008; *Le Corvec and Walter*, 2009]. Deformation of analogue models was documented for 1 h, whereas such processes are expected to take place over ~10^5 years in nature (Table 1). Assuming sediment viscosity of 10^{18} Pa s, 1 h of experiment simulates deformation in nature over 10^4 to $<10^5$ years.

4.3. Digital Image Correlation Technique

Experiments were analyzed using a digital image correlation technique (DIC). We used a commercial software package, DAVIS, distributed by La Vision Company [*LaVision*, 2002]. The DIC technique was already used in comparable analogue models in previous studies [e.g., *Adam et al*., 2005; *Burchardt and Walter*, 2009; *Le Corvec and Walter*, 2009]. This technique is used to document strain localization with submillimeter spatial resolution and detects displacements at the scale of individual sand grains [*White et al*., 2001]. For our experimental settings, spatial resolution of 0.34 and 0.25 mm was achieved for the Type I and Type II setups, respectively.

A monochrome charge-coupled device digital camera was used to acquire images at high resolution (12 megapixels). The camera was mounted on a rigid footing, and acquired images of the experiment surface at a fixed interval of 2 s for 1 h. Then the stack of 15 successive images was computed to increase the signal to noise ratio. This provided one data set every 30 s, which proved sufficient to characterize the deformation structures. For each image correlation estimation, a multiple pass correlation algorithm over multiple-pixel grid cells (i.e., typically 16×16 pixels) enabled to unambiguously follow surface patterns through successive images. Analysis of sand grain displacements between successive image pairs led to documentation of surface movements and velocities orthogonal to the camera imaging axis, and to strain derivation, precise to ~0.1 pixels [*White et al*., 2001; *Adam et al*., 2005]. In our data we are thus able to detect 0.03 mm deformation increments [*LaVision*, 2002; *Adam et al*., 2005].

Using standard postprocessing, several visual outputs can be produced from the DIC analysis, including the incremental velocity field and the displacement vector for each grid cell. From incremental displacements in the *X* and *Y* directions, normal (Exx, Eyy) and shear strain (Exy, Eyx) rates can be derived [*Adam et al*., 2005]. Cumulative shear strain best documents structures that remain stationary throughout any given experiment.

5. Analogue Modeling Experiment Results

5.1. Type I Models: Models Recorded in Cross Section

Figure 7 illustrates typical gravitational spreading as observed in the Type I experiments. As soon as the ridge is emplaced onto the flat layers, a set of two listric normal faults are generated, each dipping at ~54° outward (Figure 7). These faults accommodate outward movement of the ridge flanks, as underlying silicone flows laterally under the ridge load. For $Th_d/H_{co} \sim 0.25$ (Figure 7), the two listric faults intersect each other below the summit, defining a summit graben. With a thinner silicone layer (Th_d/H_{co} ~0.18), the listric faults intersect at the ridge summit (Figure S1 in the supporting information). As the Th_d/H_{co} is further reduced, the listric normal fault traces are observed on the flanks leaving the summit region undeformed.

Figure 7 illustrates that, for a thick silicone layer (Th_d/H_{co} ~0.25), a second set of shallow listric normal faults forms and accommodates horizontal outward displacement of lower flanks and flank slumping. Antithetic normal inward dipping faults are associated with this shallow fault system. They cause a discontinuity in the velocity field between a rapidly subsiding wedge at midflank and laterally moving lower flanks (Figure 7b). Upper and midflanks are dominated by outward rotation of entire blocks of the edifice, resulting in tilting of the surface with greater subsidence closer to the normal fault traces. Highest displacement velocities are recorded along the shallow normal faults and within a summit graben. For a thin silicone layer ($Th_d/H_{co} <0.20$), the deep outward dipping normal faults are directly associated with antithetic normal faults dipping at 60° and cutting into the midflank, forming a concave slope break at the surface (Figure S1). This pattern is similar to that observed by *Le Corvec and Walter* [2009] for spreading of half ridges over a thin silicone layer.

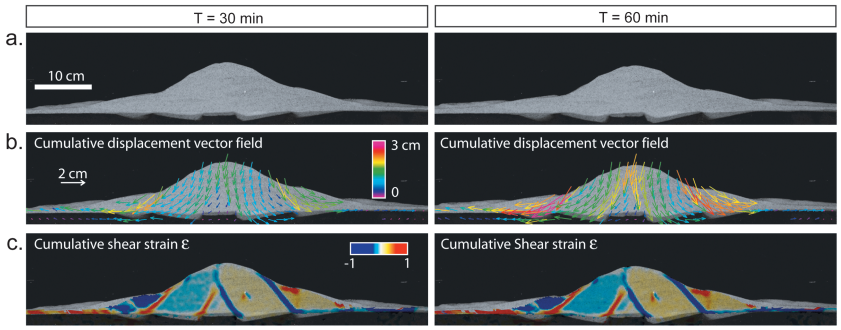

Figure 7. Lateral view of a Type I experiment with 3 cm silicone after (left column) 30 min and (right column) 60 min of deformation. (a) Raw image for the experiment; (b) cumulative displacement vector field indicating displacement direction and amplitude since deformation onset; and (c) cumulative shear strain with right lateral (blue) and left lateral (red) shear strain concentration showing two sets of normal listric faults. Two complementary normal faults cross below apex, delimiting a summit graben. Shallower outward dipping normal faults affect flanks and form steep unstable upper flanks. See Figure 10a for interpretation.

During the experiments, the silicone flows laterally, thins beneath the ridge and thickens and bulges up at the ridge base. Above the bulged silicone, the brittle material is folded. This deformation is at maximum near the ridge base but folding extends, with lower amplitude, to the model edge, 30 cm away from ridge base, after 60 min of deformation.

5.2. Type IIa Models: Uniform Models Imaged From Above

Figure 8 presents the results of a typical Type IIa experiment with a homogeneous silicone layer of uniform thickness. The initial deformation is characterized by radial deformation of the entire ridge with higher outward horizontal velocities perpendicular to the elongation axis (Figure 8b). The summit zone is not affected by horizontal displacement but subsides vertically, forming a central elongated graben. The width of this graben and the accumulated strain decreases toward the base of the elongated ridge. Cumulative volumetric strain after 20 min shows that deformation is mostly accommodated by the two arcuate structures bounding the summit graben with limited internal deformation within the flanks (Figure 8c). In all experiments, the faults bounding the central graben intersect at the base of the ridge.

As the model continues to deform, triangular wedges, separated by subvertical faults, are observed on the shear strain accumulation map (Figure 8c). The triangular wedges pointing toward the ridge summit move radially outward at a faster rate than the ones pointing toward the base of the ridge (Figure 8b). The latter displays evidence of vertical subsidence. These graben structures affect the entire long flanks but the ones closest to the middle of the ridge concentrate most of the strain. Flank slopes systematically decrease as deformation proceeds, never leading to flank instabilities.

The width of the central graben increases with time. The initial graben-bounding faults are displaced laterally as they bound the outward moving flanks. Two new conjugate faults form at a later stage within the existing graben at the initial location of the first set of faults. Significant shear strain is recorded along the graben-bounding faults indicating that these are transtensional structures rather than pure extensional ones (Figure 8c).

Beyond the ridge foot, the velocity of horizontal movements reduces radially outward (Figure 8b). This indicates the accumulation of significant, dominantly compressive, strain around the ridge base. This is associated with the subconcentric anticlines and thrusts observed in the brittle substratum near the ridge base. Cumulative strain and vertical fold amplitude are greatest at the base of the long flanks of the ridge. Deformation extends in the flat surface to a maximum distance of half the short radius of the ridge.

To evaluate the influence of relative thickness for the brittle and ductile layers upon the observed structures, a series of 23 experiments are conducted with systematic variations of the geometric ratios Th_b/Th_d, Th_b/H_{co}, and Th_d/H_{co}. Results show that a thick brittle layer ($1 < Th_b/Th_d < 3$) is associated with deformation limited to the formation of the central graben or no deformation at all ($Th_b/Th_d > 3$; see Figure S2). Irrespective of ductile layer thickness, a thick brittle crust relative to ridge height (Th_b/H_{co}) also limits or prevents any

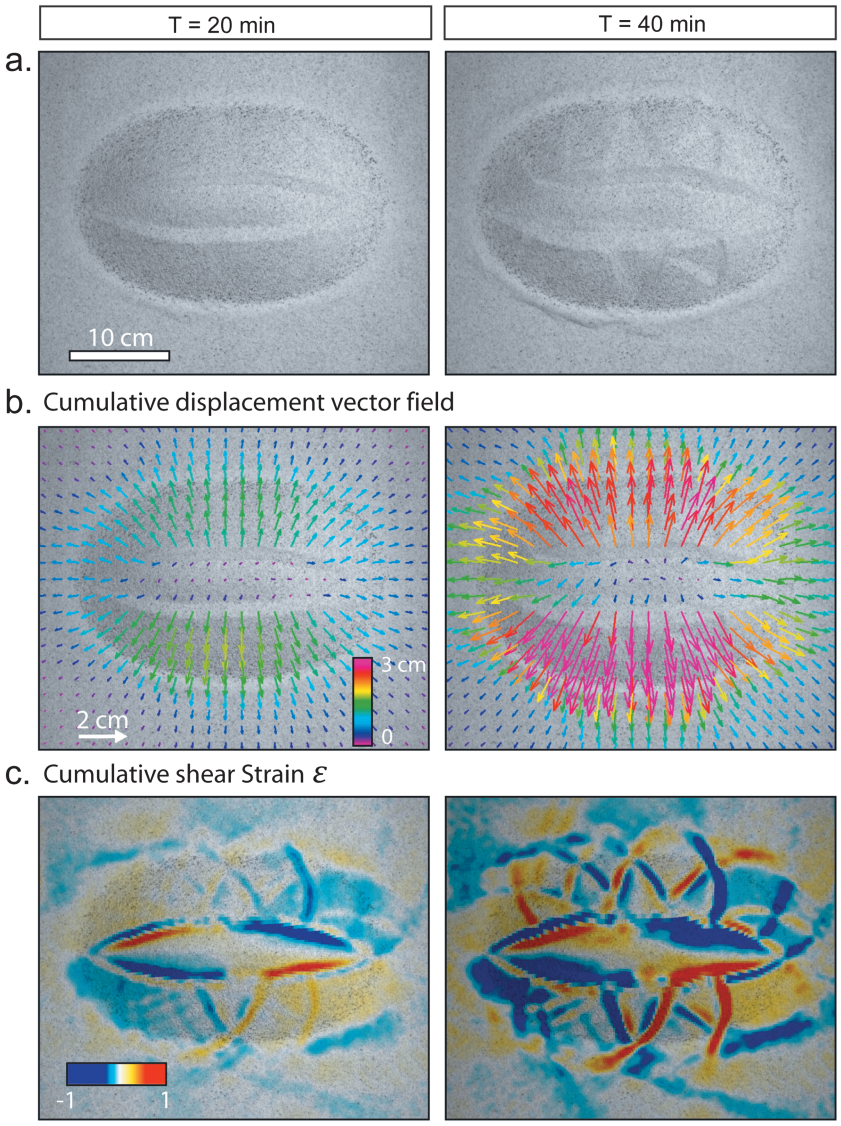

Figure 8. Plan view of a Type IIa spreading sand ridge. Silicone and sand layers are each 0.5 cm thick. Elongated ridge is 18 × 32 cm and 4.6 cm high. (a) Image of model after 20 min (left column) and 40 min (right column) of deformation; (b) cumulative displacement vector field indicating displacement direction and amplitude since deformation onset; and (c) cumulative shear strain with right lateral (blue) and left lateral (red) shear strain concentration highlighting strike-slip faults bordering the main central graben and smaller V-shaped grabens on the flanks. See Figure 10b for interpretation.

gravitational deformation. A very thick ductile layer ($Th_b/Th_d < 0.1$) induces vertical sagging of the ridge into the ductile basement, causing compressive stresses along the flank and extensional fractures around its base [see *Kervyn et al.*, 2010; *Byrne et al.*, 2013].

5.3. Type IIb Model: Ductile Layer of Nonuniform Thickness

Figure 9 illustrates the deformation of Type IIb models in which a narrow silicone band is placed orthogonal to the ridge axis with a lower thickness below the ridge than under the lower flanks and flat base (Figures 6b and 6c). The deformation is restricted to the segment of the ridge built over the silicone layer and is controlled by two sets of symmetric listric faults formed simultaneously. The deepest faults border a narrow summit graben. The second set of faults accommodates the faster outward movements of the lower flanks associated with the formation of unstable upper flanks (Figure 9). The shallow faults' position is controlled by the position of the step in silicone thickness. Both sets of faults have a dominant normal component in their central part and turn into strike-slip structures at the lateral edge of the deforming flanks

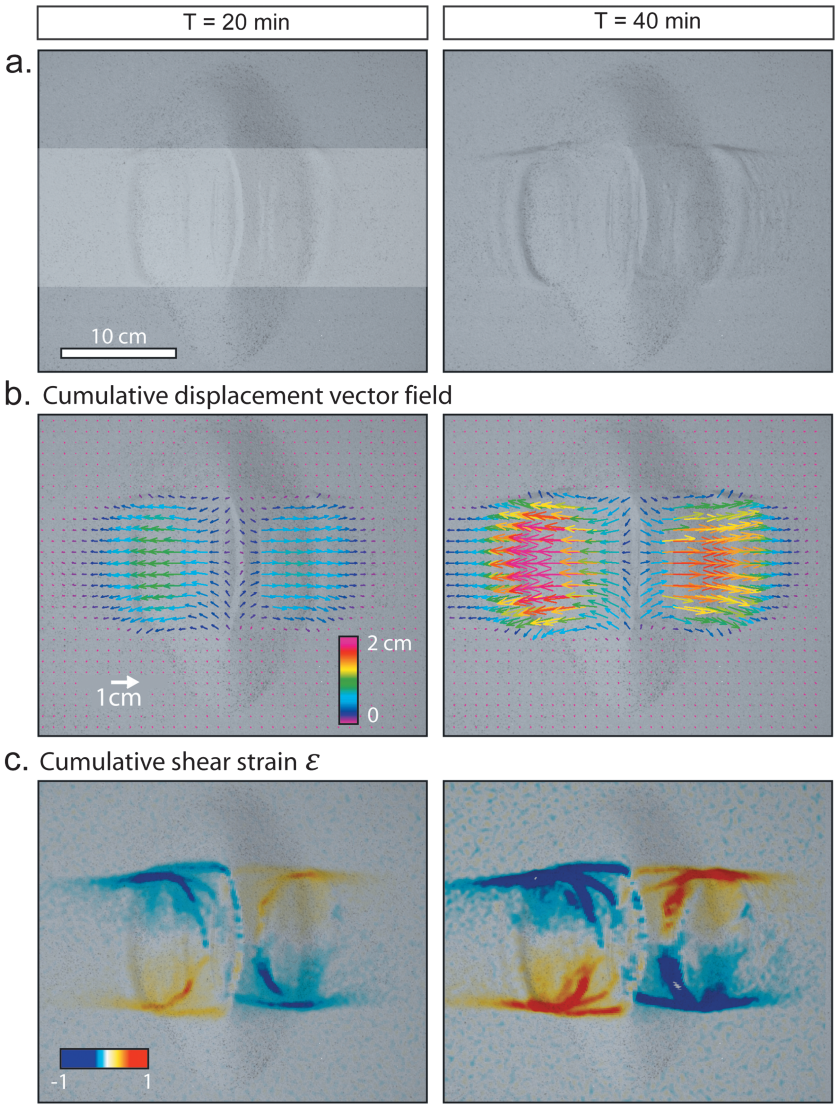

Figure 9. Plan view of a Type IIb experiment with nonuniform silicone layer. A 15 cm band of silicone is emplaced perpendicular to the ridge axis (white rectangle in Figure 9a), below its central part. Silicone is 4 and 12 mm thick below the ridge central part and lower flank and base, respectively. (a) Image of model after 20 min (left column) and 40 min (right column) of deformation; (b) cumulative displacement vector field indicating displacement direction and amplitude since deformation onset; and (c) cumulative shear strain with right lateral (blue) and left lateral (red) shear strain concentration along strike-slip faults. See Figure 10c for interpretation.

(Figure 9). The shallow faults have subcircular surface traces, whereas a sharper transition in structure orientations is recorded for the deeper faults (Figure 10c).

The extent of the summit graben is bounded by the intersection of the two deep normal faults with opposite dip orientation. The long axis of the summit graben matches with the lateral extent of the deforming flanks. As flanks are constantly moving outward, whereas strain localization is observed to be stationary, several faults form successively, creating several topographic steps at the edges of the summit graben (Figures 9 and 10c).

Sharp topographic steps at intermediate height within the deforming flanks are identified at the experiment onset. These suggest the presence of inward dipping antithetic faults associated with the deeper faults when movement is faster along the deeper graben-bounding faults. As deformation progresses strain concentrates on the flanks, with less deformation along graben-bounding faults (Figure 9). Antithetic faults are no longer active but remain as topographic steps in the lower flanks.

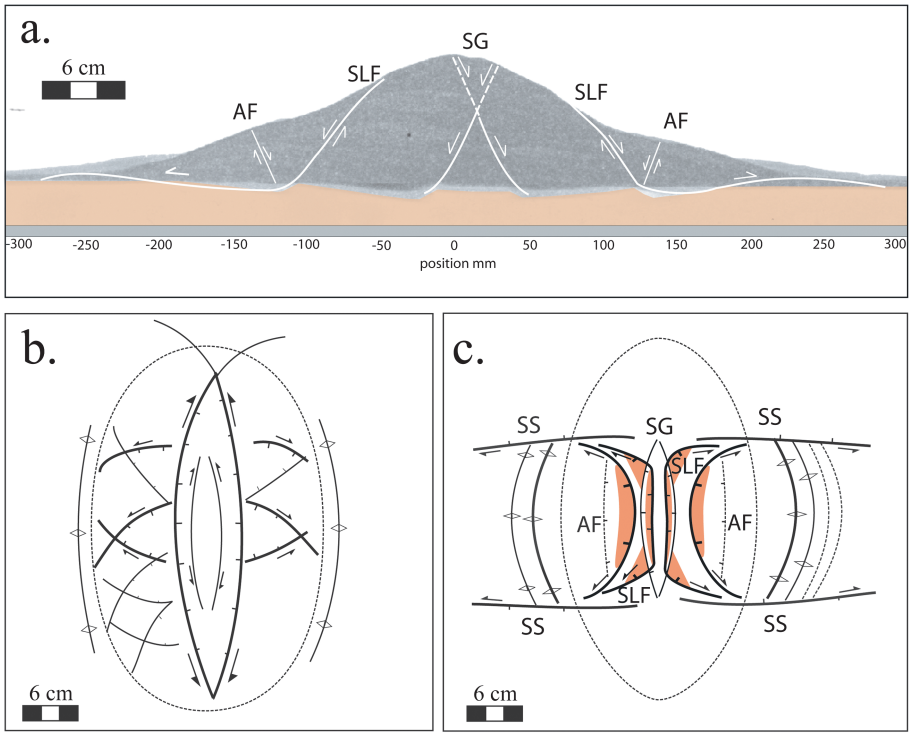

Figure 10. Interpretation sketches for the analogue models presented in Figures 7–9. (a) Type I model: spreading of a sand ridge between glass panes over 3 cm of silicone as presented in Figure 7. (b) Type IIa model: spreading sand ridge presented in Figure 8; and (c) Type IIb model: spreading of a sand ridge over a nonuniform ductile layer as presented in Figure 9; SG: summit graben; SS: strike-slip fault; SLF: shallow listric fault; and AF: antithetic fault. Orange color: steep unstable slopes.

Destabilization of the flanks by shallow slumps is observed when the lower flanks are spreading outward, along the shallow faults, faster than the upper flanks, along the deeper faults. Such dynamics is only obtained when the silicone layer is thinner below the ridge than below the lower flanks and flat substratum. When the silicone thickness is homogeneous, the deformation along the deeper faults is faster and do not result in the formation of unstable flanks.

Shear strain localization along linear structures striking downslope points to the formation of strike-slip faults relaying the summit graben edges to the deforming lobes at the base of the ridge (Figures 9 and 10). Material folding and thrusting within the flat base occur in the direction perpendicular to the ridge's elongation axis and extend to greater distances from the base than observed in Type IIa experiments. Folds and thrusts have a parabolic outline with significant strain accumulation in the brittle layer at the lateral edge of the silicone band (Figure 9): these lateral edges are marked by topographic steps caused by uplift of the deforming zone relative the stable substratum.

Relative position and interactions of the shallow fault on one flank and the deep listric fault dipping in the opposite direction are responsible for complex topographic irregularities along the summit zone. The initial position of the different fault structures depends on the thickness distribution and the width of the silicone layer accommodating the deformation.

6. Discussion

6.1. Morphostructural Interpretation

The faults and folds obtained in analogue models, as well as the morphology of the deformed ridges, are here compared with the structural map and surface morphology of Mount Cameroon (Figures 5 and 10).

For the models in cross section (Type I, Figure 10a), lateral flank spreading results in an uneven flank slope distribution with steep slopes being formed at midflanks by the shallow listric normal faults and flatter terrains on the lower flanks associated to antithetic faults. Toward the summit, a flat graben is formed by intersection of

Table 2. Comparison of Morphostructural Features Observed at Mount Cameroon and Those Reproduced by the Three Sets of Analogue Models[a]

Morphostructural Features of Mount Cameroon	Type I	Type IIa	Type IIb	Rift Zone Intrusion [*Le Corvec and Walter*, 2009][b]
Steep unstable long flanks	V	X	V	(V)
Linear SE flank	(V)	X	V	(V)
Convex NW flank + Elephant Valley	X	X	X	X
Sharp break-in-slope at base of steep flanks	V	X	V	(V)
Fault bounded elliptical summit plateau	(V)	X	V	(V)
Undeformed lower flanks along rift zone	X	X	V	(V)
Parabolic sediment ridges subparallel to volcano long flanks	(V)	V	V	X
Strike-slip faults orthogonal to elongation axis	X	(V)	V	X

[a]See text for discussion. V, feature reproduced by experiment; (V), feature partially reproduced or consistent if Type I models are extrapolated in 3-D; and X, feature not reproduced.
[b]The deformation caused by rift zone intrusion is evaluated from experiments illustrated in *Le Corvec and Walter* [2009]: locally unstable flanks are formed only for shallow intrusions whereas basal thrusts and folds are associated with deep intrusion and do not extend beyond the cone base.

the two main listric normal faults. The resulting edifice profile for such a faulting configuration is very similar to that observed at Mount Cameroon, with a flat summit zone bounded by normal faults, steep upper flanks, and low angle lower flanks turning into a far-reaching folded basal zone (Table 2 and Figure 10a).

In experiments recorded from above with a homogeneous ductile layer (Type IIa and Figure 10b), gravitational stresses cause radially outward flow of the silicone initially located below the ridge. This induces a radial spreading of the ridge and the formation of V-shaped grabens on the ridge flanks. These features are similar to grabens observed in experiments simulating the spreading of axisymmetric cones [*Merle and Borgia*, 1996; *Delcamp et al*., 2008; *Kervyn et al*., 2010]. The gravitational stress gradient is larger orthogonal to the long axis of the ridge. The lateral spreading thus occurs at a faster rate in that direction, leading to a better developed summit graben and more extensive basal deformation orthogonal to the long axis. Radial dissipation of the compressive strain away from the ridge's base limits the extent of the thrusts and folds affecting the flat surface. The extent of the summit graben, the occurrence of spreading-related grabens on the long flanks, and the absence of steep slopes do not match with the observed morphology of Mount Cameroon (Table 2).

In the third set of experiments with a nonhomongeneous ductile layer (Type IIb, Figure 10c), the spreading is laterally constrained by the extent of the ductile layer. This results in the unidirectional spreading of the long flanks in a direction orthogonal to the ridge's long axis. The shear stress at the edge of the spreading flanks causes the listric normal faults to turn downslope into strike-slip faults, separating the deformation of the spreading flanks from the stable part of the ridge. The deep listric normal faults border a narrow summit graben which length is limited to that of the spreading flanks. Faster outward spreading of the lower flanks, due to variation in ductile layer thickness, leads to the formation of additional outward dipping listric normal faults which are associated with the formation of steep and unstable slopes on the upper flanks. Deformation beyond the base of the ridge extends to a great distance but is limited to a parabolic-shaped area adjacent to the spreading flanks. This Type IIb model best reproduces the features observed at Mount Cameroon (Table 2). Therefore, we deduce that the deformation dynamics and velocity fields documented for this type of analogue model (Figures 9 and 10) best represent the long-term dynamics of gravitational deformation at Mount Cameroon.

6.2. Mount Cameroon—A Spreading Volcano

From interpretation of topographic and volcano-tectonic structures and from comparison with analogue models, we propose an interpretative model in which Mount Cameroon deforms over ductile sediments (Figure 11c). The structure of the sedimentary basins, with the stepwise sediment thickening toward SSW and increased occurrence of clay-rich layers in the Tertiary sediments, is interpreted as responsible for restriction of spreading to the central part of Mount Cameroon. Only in that zone is the load sufficient and the ductile layer present at a favorable depth to cause outward ductile sediment flow and associated flank spreading. The sharp lateral limit for basal deformation NW of the volcano, along a N125°E linear feature, is consistent with this interpretation: the different parts of the sedimentary basins are separated by N120–135°E normal faults dipping SW [e.g., *Regnoult*, 1986; *Moreau et al*., 1987].

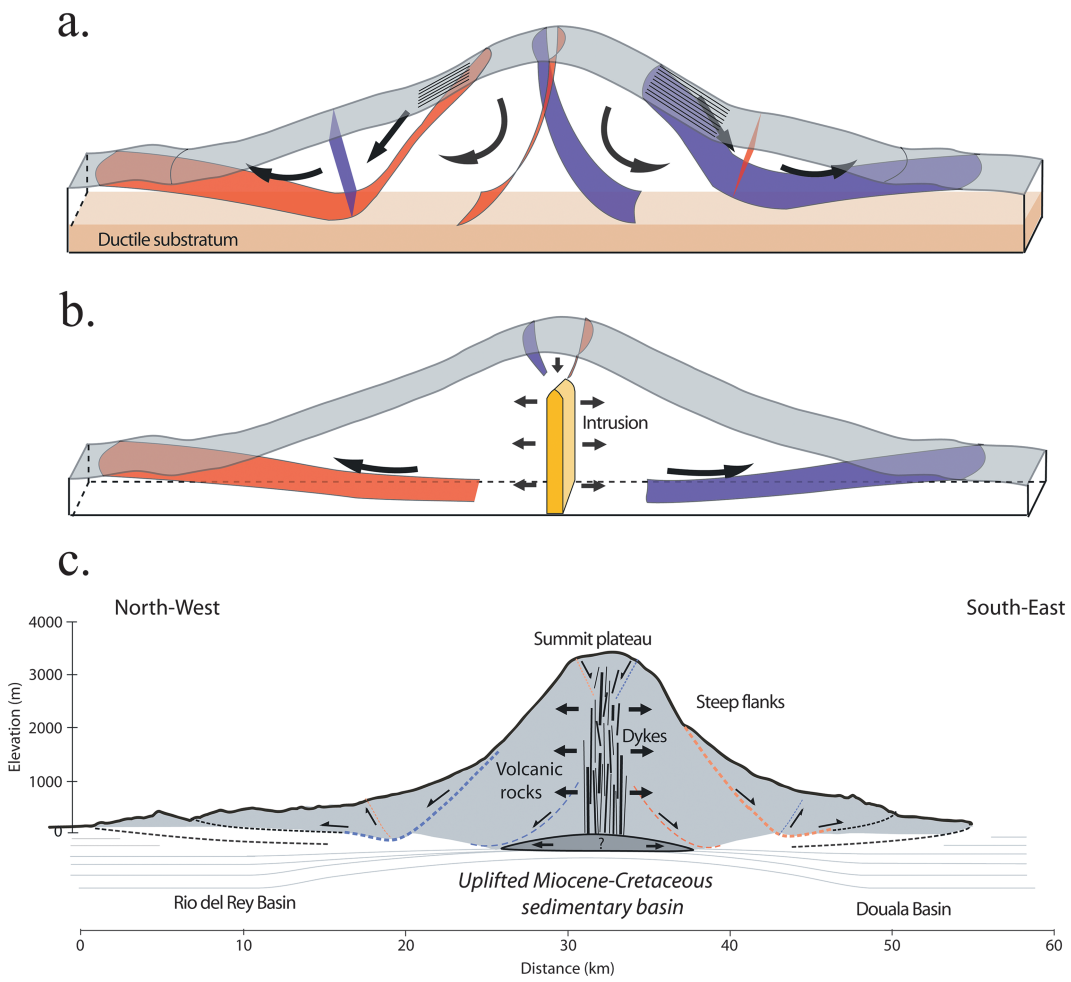

Figure 11. Conceptual sketches of two end-member deformation structures induced by (a) gravitational spreading, based on experimental results presented in this paper, and (b) volcanic rift zone intrusions modeled by *Le Corvec and Walter* [2009]. (c) Interpretation of Mount Cameroon cross-section orthogonal to the elongation axis shown in Figure 2c illustrating the position of, and movement along faults as interpreted from analogue modeling (adapted from *Mathieu et al.* [2011]). Vertical scale is exaggerated 3 times for better clarity.

Analogue models suggest that a summit graben and steep upper flanks can only coexist at Mount Cameroon if there are differential outward spreading velocities between lower flanks and summit area. Such differential spreading can arise when the depth or thickness of ductile sediments varies across the volcanic axis or if a buttress exists in the underground, hindering spreading in one or some directions [*Walter*, 2003]. Such an interpretation is consistent with offshore observations of uplifted Miocene crust by *Meyers et al.* [1998]. Assuming that such crustal uplift also affected Mount Cameroon basement in the Miocene, the lower thickness of ductile material below the volcano central zone causes slow movement along the deep normal faults accommodating summit subsidence, and more rapid movement of the outer flank, which overlies thicker sediments. The striking slope breaks observed at the base of the steep upper flanks are also interpreted here as the topographic expression of antithetic faults associated with shallow listric normal faults (Figure 2). Repetitive dyke intrusions along the rift zone are expected to contribute to oversteepening of the upper flanks when emplaced at shallow depth and may contribute to the subsidence of the summit graben.

There is a noticeable absence of structures or other evidence of deformation affecting the NE and SW flanks of Mount Cameroon. NE of the spreading sector, the underlying sediments are mostly composed of less readily deformable Cretaceous siltstones and sandstones. The limited extent of the NE volcanic rift zone is consistent with the absence of extensional strain to the NE. To the SW, the presence of the older Limbe-

Mabeta volcanic massif and of Mount Etinde volcano can potentially act as local buttressing, limiting the potential deformation of the volcano in that area. The flank may not be wide enough to overlay the thicker sediment. The broad extent of the eruptive fissures to low elevations, however, suggests that extensional strain is greater on the SW flank relative to the NE flank. Finally, the overall absence of V-shaped grabens perpendicular to the elongation axis—with the noticeable exception of the Elephant Valley—suggests that no or limited spreading is taking place parallel to the volcano long axis, due to presence of the stable SE and NW flanks of Mount Cameroon.

6.3. Limitations of the Analogue Models

A thorough comparison of the analogue models with Mount Cameroon architecture is prevented by the lack of geophysical data. Existing seismic evidence is however consistent with the proposed model [*Ambeh et al*., 1989; *Ateba and Ntepe*, 1997; *Ubangoh et al*., 1997]. Most earthquakes recorded in the 1980s were single events or swarms below the two spreading sectors. To the NW, earthquakes occurred at less than 10 km depth [*Ambeh et al*., 1989]. Interestingly, seismic swarms below the spreading flanks are more common during the rainy season [*Ubangoh et al*., 1998]. Although the accuracy of hypocenter localization is insufficient to draw definitive conclusions, such earthquake swarms are consistent with movement of the unstable flanks along one or several decollement surfaces within the sedimentary deposits. Existing field evidence at Mount Cameroon presented by *Mathieu et al*. [2011] is also consistent with the model proposed here.

Table 2 highlights that the only topographic feature of Mount Cameroon that is not properly accounted for by our conceptual model (Figure 11) and not reproduced by our analogue experiments is the presence of the Elephant Valley and its surrounding outward topographic bulge within the steep NE flank. Our model does not confirm, or invalidate, previously proposed explanations for the formation of this valley: e.g., glacial erosion [*Déruelle et al*., 1987], radial spreading [*Suh et al*., 2003], or extensional stresses associated with the rotation of a large block within the flank [*Mathieu et al*., 2011]. The fresh nature and steep slopes of the Elephant Valley wall suggest that it is a recent or still-active morphological structure. We hypothesize that an interplay of differential outward spreading velocities within the flank, a tectonic discontinuity orthogonal to Mount Cameroon elongation, and cutting across the volcano, and/or an asymmetry in magmatic forcing might have contributed to create the local topographic bulge within the NE flank. Such deformation could then have triggered flank destabilization, local extensional stresses, or concentrated erosion to carve the Elephant Valley itself. Further geophysical and structural investigations in the field are required to unravel the origin of this valley.

Our model does not take into account the potential effect of regional tectonics upon the deformation at Mount Cameroon. This is made difficult by the lack of constraints on the activity and dynamics of documented tectonic structures in the region, the main ones being oriented N030°E, N050°E to N070°E, and N000°E and N130°E [*Moreau et al*., 1987]. Other processes are also neglected in our models: (i) heterogeneous rock properties within the sediment substrata or within the volcano, e.g., presence of a shallow magma reservoir or a dyke core complex below the central rift zone, (ii) possible non-Newtonian rheology of the ductile layer, and (iii) gradual—instead of instantaneous—growth of the volcano load.

Moreover, the analogue models focus on gravitational deformation (Figure 11a) and do not reproduce the contribution of magma intrusions to Mount Cameroon deformation and structure. Magma storage into a shallow reservoir (i.e., $<$5 km depth) and repetitive subvertical dyke emplacement within the main rift zone is expected to be associated with significant volcano deformation. *Le Corvec and Walter* [2009] showed that such rift zone intrusions is associated with graben formation above the dyke complex and outward flank displacement along a subhorizontal fault at the level of the intrusion base (Figure 11b and Table 2). This outward movement of a coherent flank leads to localized flank steepening and shallow instability for intrusions initiated at shallow depth, or to thrusting of the flank base if the deformation was accommodated by a deep decollement (Figure 11b), but both features were not reproduced simultaneously. Combined gravitational spreading and intrusion was also shown to be sometimes associated with subdued expression of the spreading-related listric faults.

It is expected that repetitive dyke injection along the central rift zone of Mount Cameroon plays an important role in its structure and deformation. Formation of a dyke complex might have contributed to the formation of a central graben although its limited longitudinal extent relative to the distribution of eruptive vents

suggests that intrusion-induced deformation cannot account for it alone. Dyke intrusions at shallow level might also have contributed to oversteepening and destabilization of upper flanks, although there is no evidence for a shallow source of intrusion within Mount Cameroon [*Suh et al*., 2003]. Unraveling the relative importance of intrusion-induced destabilization relative to that caused by gravitational deformation at Mount Cameroon remains a challenge as the frequency of intrusions and the velocity of flank spreading between intrusive events is not yet constrained. However, the limited extent of the summit graben and the striking correspondence between fault locations and types with gravitationally induced structures in analogue models suggests that Mount Cameroon is spreading under gravity faster than it is being pushed by forceful intrusions.

6.4. Analogue for Flank Slumps at Other Volcanoes

All of Mount Cameroon's deformation-related structures are visible on land. Many other large volcanic constructs are either oceanic islands (e.g., Hawaii, Piton de la Fournaise) or built on the shoreline (e.g., Etna). Deformation structures affecting the lower flanks at these other volcanoes are thus more difficult to map. Several of these volcanoes show strong evidence for continuous, usually asymmetric, flank spreading driven by gravity and/or repeated magmatic intrusions [see *Le Corvec and Walter*, 2009], sometimes in interaction with tectonic faulting (e.g., Etna) [*Le Corvec et al*., 2014]. Processes documented here—i.e., laterally constrained flank spreading, associated with summit subsidence, and shallow slumps affecting upper slopes due to differential spreading velocity of the lower flanks—are expected to similarly apply to some of these structures where both summit subsidence and flank slumping (e.g., Hilina Pali faults, Kilauea) [*Morgan et al*., 2003] or sector collapses are observed simultaneously [*Oehler et al*., 2005]. Similar processes are also expected to occur at extraterrestrial volcanoes: e.g., *Platz et al*. [2011] inferred a variation in substratum rheology to account for the unidirectional flank spreading of Tharsis Tholus on Mars, resulting in a comparable morphology as that of Mount Cameroon. The exact dynamics of the process and source of the differential movement for lower flank is however expected to vary with the local setting.

7. Conclusions

Analogue models presented here provide insights into the complex deformation structures documented at Mount Cameroon from morphostructural analysis of the SRTM digital elevation model and from field evidence [*Mathieu et al*., 2011]. Directional spreading of the central part of the volcano over the underlying sedimentary basins is proposed to be largely responsible for the observed structures, although repetitive dyke intrusions along the rift zone certainly contribute to the overall deformation pattern and structures. Variations of the sediment thickness and properties across the Cameroon Volcanic Line, associated with crustal uplift, can account for differential movement of the lower flanks, creating simultaneously a flat summit graben, unstable upper slopes, and far reaching basal folds and faults.

This deformation model for Mount Cameroon has implications for nonmagmatic earthquakes and slope instability hazards (see *Bonne et al*. [2008] and *Thierry et al*. [2008] for further discussion of hazards at Mount Cameroon). Repeated slope instabilities are likely to affect the steep upper flanks, and to potentially affect densely inhabited areas (e.g., Buea). Seismic activity associated with flank spreading along the strike-slip faults (e.g., Bokosso faults) or underneath the spreading flanks is also likely to pose a seismic hazard outside eruptive periods [see *Ubangoh et al*., 1997]. The presented analogue models also provide insights for other volcanoes where large-scale flank spreading and summit subsidence are associated with localized flank instabilities.

Mount Cameroon has been increasingly studied since the 1999 and 2000 eruptions, and there is now an opportunity to start characterizing its deformation dynamics and magmatic system systematically. Further studies are needed to quantify the rate of movement of the well-expressed faults bordering the summit plateau and the Bokosso faults, to unravel effects of magma intrusion and the origin of the Elephant Valley. This can be achieved by applying ground-based (broadband seismometer array, GPS, and gravimetry) and spaced-based geophysical methods (synthetic aperture radar interferometry) during and in-between eruptive periods. Specific field studies to document the Elephant Valley floor and wall deposits systematically would be beneficial. Such studies at Mount Cameroon would be well suited and timely to help advance the understanding of large basaltic volcanoes, and would also contribute to quantifying hazards and risks at this densely populated volcano.

Acknowledgments

Data from analogue models presented in this manuscript are available upon request to M.K. Comments on a preliminary version of this manuscript by L. Mathieu and A. Delcamp, and reviews by A. Tibaldi, N. Le Corvec, and A. Borgia greatly helped to improve this article. M.K. and G.G.J.E. partly conducted this research during their postdoctoral at Ghent University with the support of the *Fonds voor Wetenschappelijk Onderzoek—Vlaanderen*. Experimental results were obtained during research stays of M.K. at LMV and GFZ, thanks to financial support by FWO and Blaise Pascal University. We are grateful to Onno Oncken for granting access to the GFZ analogue lab. We acknowledge technical assistance and stimulating discussions with many researchers and students in those labs, especially Lucie Mathieu, Matthias Roseneau, and David Boutelier. This research was conducted in the framework of the VLIR Own Initiative project entitled *Capacity building in geohazards monitoring in volcanically active areas of SW Cameroon* between UGhent and UBuea. We finally acknowledge collaboration and support of staff and students at the DGES of UBuea during fieldwork.

References

Adam, J., J. Urai, B. Wienecke, O. Oncken, K. Pfeiffer, N. Kukowski, J. Lohrmann, S. Hoth, W. Van Der Zee, and J. Schmatz (2005), Shear localization and strain distribution during tectonic faulting—New insights from granular-flow experiments and high resolution optical image correlation techniques, *J. Struct. Geol.*, *27*, 283–301.

Ambeh, W. B., J. D. Fairhead, D. J. Francis, J. M. Nnange, and D. Soba (1989), Seismicity of the Mount Cameroon region, West Africa, *J. Afr. Earth Sci.*, *9*, 1–7.

Ateba, B., and N. Ntepe (1997), Post-eruptive seismic activity of Mount Cameroon (Cameroon), West Africa: A statistical analysis, *J. Volcanol. Geotherm. Res.*, *79*, 25–45.

Ateba, B., C. Dorbath, L. Dorbath, N. Ntepe, M. Frogneux, F. T. Aka, J. V. Hell, J. C. Delmond, and D. Manguelle (2009), Eruptive and earthquake activities related to the 2000 eruption of Mount Cameroon volcano (West Africa), *J. Volcanol. Geotherm. Res.*, *179*, 206–216.

Belmonte, Y. C. (1966), Stratigraphie du bassin sédimentaire du Cameroun, paper presented at Second West African Micropaleontological Colloquium, Ibadan.

Benkhelil, J., P. Giresse, C. Poumot, and G. Ngueutchoua (2002), Lithostratigraphic, geophysical and morpho-tectonic studies of the South Cameroon shelf, *Mar. Pet. Geol.*, *19*(4), 499–517.

Bonne, K., M. Kervyn, L. Cascone, S. Njome, E. Van Ranst, E. Suh, S. Ayonghe, P. Jacobs, and G. G. J. Ernst (2008), A new approach to assess long-term lava flow hazard and risk using GIS and low cost remote sensing: The case of Mount Cameroon, West Africa, *Int. J. Remote Sens.*, *29*, 6539–3564.

Borgia, A., L. Ferrari, and G. Pasquarè (1992), Importance of gravitational spreading in the tectonic and volcanic evolution of Mount Etna, *Nature*, *357*(6375), 231–235.

Borgia, A., P. T. Delaney, and R. P. Denlinger (2000), Spreading volcanoes, *Annu. Rev. Earth Pl. Sc.*, *28*, 539–570.

Brownfield, M. E., and R. R. Charpentier (2006), Total petroleum systems, West-Central coastal Province, West Africa, *USGS Geol. Surv. Bull.*, *2207-B*, 1–52.

Burchardt, S., and T. R. Walter (2009), Propagation, linkage, and interaction of caldera ring-faults: Comparison between analogue experiments and caldera collapse at Miyakejima, Japan, in 2000, *Bull. Volcanol.*, doi:10.1007/s00445-00009-00321-00447.

Byrne, P. K., E. P. Holohan, M. Kervyn, B. V. de Vries, V. R. Troll, and J. B. Murray (2013), A sagging-spreading continuum of large volcano structure, *Geology*, *41*(3), 339–342.

Byrne, P. K., E. P. Holohan, M. Kervyn, B. van Wyk de Vries, and V. R. Troll (2014), Analogue modelling of volcano flank terrace formation on Mars, *Geol. Soc. London Spec. Publ.*, doi:10.1144/SP1401.1114.

Chiarelli, A. (1976), Étude des nappes aquiferes profondes du bassin de Douala, Cameroun. Study of the deep aquifers of Douala Basin, Cameroon, in *Hydrogeology of Great Sedimentary Basin, Proceeding of the International Hydrogeological Conference, Budapest, Hungary*, edited by R. Andras et al., p. 322, Budapest.

Delaney, P. T. (1992), Volcanoes—You can pile it only so high, *Nature*, *357*(6375), 194–196.

Delcamp, A., B. V. de Vries, and M. R. James (2008), The influence of edifice slope and substrata on volcano spreading, *J. Volcanol. Geotherm. Res.*, *177*(4), 925–943.

Déruelle, B., J. Nni, and R. Kambou (1987), Mount Cameroon—An active volcano of the Cameroon Line, *J. Afr. Earth Sci.*, *6*(2), 197–214.

Déruelle, B., I. Ngounouno, and D. Demaiffe (2007), The "Cameroon hot line": A unique example of active alkaline intraplate structure in both oceanic and continental lithosphere, *C. R. Geosci.*, *339*, 589–600.

Dieterich, J. H. (1988), Growth and persistence of Hawaiian volcanic rift zones, *J. Geophys. Res.*, *93*(B5), 4258–4270, doi:10.1029/JB093iB05p04258.

Dumort, J. C. (1968), *Notice Explicative de la Feuille Douala Ouest avec carte gélogique au 1/500 000*, Dir. Mines Géol, Cameroon.

Dzurisin, D. (2007), *Volcano Deformation: Geodetic Monitoring Techniques*, 441 pp., Springer, Berlin.

Fiske, R. S., and E. D. Jackson (1972), Orientation and growth of Hawaiian volcanic rifts: The effect of regional structure and gravitational stresses, *Proc. Roy. Soc. Lond. A*, *329*, 299–326.

Fitton, J. G., C. R. J. Kilburn, M. F. Thirlwall, and D. J. Hughes (1983), 1982 Eruption of Mount Cameroon, West-Africa, *Nature*, *306*(5941), 327–332.

Gallacher, R. J., and I. D. Bastow (2012), The development of magmatism along the Cameroon Volcanic Line: Evidence from teleseismic receiver functions, *Tectonics*, *31*, doi:10.1029/2011TC003028.

Gèze, B. (1943), Géographie physique et géologie du Cameroun occidental, *Mémoire du Muséum National d'Histoire*, *17*, 1–272.

Grosse, P., B. V. de Vries, I. A. Petrinovic, P. A. Euillades, and G. E. Alvarado (2009), Morphometry and evolution of arc volcanoes, *Geology*, *37*(7), 651–654.

Hedberg, J. D. (1968), A geological analysis of the Cameroon trend, PhD thesis, 154 pp., Princeton Univ., Princeton.

Hoek, E., C. Carranza-Torres, and B. Corkum (2002), Hoek-Brown failure criterion—2002 Edition, paper presented at Proceeding North American Rock Mechanics Society - TAC Conference, Toronto.

Kervyn, M., M. Boone, B. van Wyk de Vries, E. Lebas, V. Cnudde, K. Fontijn, and P. Jacobs (2010), 3D imaging of volcano gravitational deformation by computerized X-ray micro-tomography, *Geosphere*, *6*(5), 482–498, doi:10.1130/GES00564.1.

LaVision (2002), *StrainMaster Manual for DaVis 6.2*, LaVision GmbH, Goettingen.

Le Corvec, N., and T. R. Walter (2009), Volcano spreading and fault interaction influenced by rift zone intrusions: Insights from analogue experiments analyzed with digital image correlation technique, *J. Volcanol. Geotherm. Res.*, *183*(3–4), 170–182, doi:10.1016/j.jvolgeores.2009.02.006.

Le Corvec, N., T. R. Walter, J. Ruch, A. Bonforte, and G. Puglisi (2014), Experimental study of the interplay between magmatic rift intrusion and flank instability with application to the 2001 Mount Etna eruption, *J. Geophys. Res. Solid Earth*, *119*, 5356–5368, doi:10.1002/2014JB011224.

Le Maréchal, A. (1975), *Carte géologique de l'Ouest du Cameroun et de l'Adamaoua, 1:1000000, ORSTOM, Office de la Recherche Scientifique et Technique d'Outre-mer*, Bondy, France.

Lohrmann, J., N. Kukowski, J. Adam, and O. Oncken (2003), The impact of analogue material properties on the geometry, kinematics and dynamics of convergent sand wedges, *J. Struct. Geol.*, *25*, 1691–1711.

Marzoli, A., E. M. Piccirillo, P. R. Renne, G. Bellieni, M. Iacumin, J. B. Nyobe, and A. T. Tongwa (2000), The Cameroon line revisited: Petrogenesis of continental basaltic magmas from lithospheric and asthenospheric mantle sources, *J. Petrol.*, *41*, 87–109.

Mathieu, L., and B. van Wyk de Vries (2009), Edifice and substrata deformation induced by intrusive complexes and gravitational loading in the Mull volcano (Scotland), *Bull. Volcanol.*, *71*(10), 1133–1148.

Mathieu, L., M. Kervyn, and G. G. J. Ernst (2011), Field evidence for flank instability, basal spreading and volcano-tectonic interactions at Mt Cameroon, West Africa, *Bull. Volcanol.*, *73*(7), 851–867, doi:10.1007/s00445-00011-00458-z.

McGovern, P. J., and J. K. Morgan (2009), Volcanic spreading and lateral variations in the structure of Olympus Mons, Mars, *Geology*, *37*(2), 139–142.

Merle, O., and A. Borgia (1996), Scaled experiments of volcanic spreading, *J. Geophys. Res.*, *101*(B6), 13,805–13,817, doi:10.1029/95JB03736.
Meyers, J. B., and B. R. Rosendahl (1991), Seismic-reflection character of the Cameroon Volcanic Line—Evidence for uplifted oceanic-crust, *Geology*, *19*(11), 1072–1076.
Meyers, J. B., B. R. Rosendahl, H. Groschel-Becker, J. Austin, and P. A. Rona (1996), Deep penetrating MCS imaging of the rift-to-drift transition, offshore Douala and North Gabon basins, West Africa, *Mar. Pet. Geol.*, *13*(7), 791–835.
Meyers, J. B., B. R. Rosendahl, C. G. A. Harrison, and Z. D. Ding (1998), Deep-imaging seismic and gravity results from the offshore Cameroon volcanic line, and speculation of African hotlines, *Tectonophysics*, *284*(1–2), 31–63.
Milelli, L., L. Fourel, and C. Jaupart (2012), A lithospheric instability origin for the Cameroon Volcanic Line, *Earth Planet. Sci. Lett.*, *335*, 80–87.
Moreau, C., J. M. Regnoult, B. Deruelle, and B. Robineau (1987), A new tectonic model for the Cameroon Line, Central-Africa, *Tectonophysics*, *141*(4), 317–334.
Morgan, J. K., G. F. Moore, and D. A. Clague (2003), Slope failure and volcanic spreading along the submarine south flank of Kilauea volcano, Hawaii, *J. Geophys. Res.*, *108*(B9), 2415, doi:10.1029/2003JB002411.
Njome, M. S., C. E. Suh, R. S. J. Sparks, S. N. Ayonghe, and J. G. Fitton (2008), The Mount Cameroon 1959 compound lava flow field: Morphology, petrography, geochemistry, *Swiss J. Geosci.*, *101*, 85–98.
Oehler, J. F., B. V. de Vries, and P. Labazuy (2005), Landslides and spreading of oceanic hot-spot and arc shield volcanoes on Low Strength Layers (LSLs): An analogue modeling approach, *J. Volcanol. Geotherm. Res.*, *144*(1–4), 169–189.
Panien, M., G. Schreurs, and A. Pfiffner (2006), Mechanical behaviour of granular materials used in analogue modeling: Insights from grain characterization, ring-shear-tests and analogue experiments, *J. Struct. Geol.*, *28*, 1710–1724.
Platz, T., S. Münn, T. R. Walter, J. N. Procter, P. C. McGuire, A. Dumke, and G. Neukum (2011), Vertical and lateral collapse of Tharsis Tholus, Mars, *Earth Planet. Sci. Lett.*, *305*(3–4), 445–455.
Ponsard, J. F., and L. Saugy (1989), Structures associées à la marge continentale du Nigéria d'après l'étude du magmatisme, *Comptes Rendus de l'Académie des Sciences*, *308*, 627–634.
Poudjom Djomani, Y. H., M. Diament, and M. Wilson (1997), Lithospheric structure across the Adamawa plateau (Cameroon) from gravity studies, *Tectonophysics*, *273*, 317–327.
Ramberg, H. (1981), *Gravity, Deformation and the Earth's Crust in Theory, Experiments and Geologic Application*, 2nd ed., 452 pp., Academic Press, London.
Regnoult, J. M. (1986), *Synthèse géologique du Cameroun*, 119 pp., Ministère des Mines et de l'Energie, Yaoundé.
Reusch, A. M., A. A. Nyblade, D. A. Wiens, P. J. Shore, B. Ateba, C. T. Tabod, and J. M. Nnange (2010), Upper mantle structure beneath Cameroon from body wave tomography and the origin of the Cameroon Volcanic Line, *Geochem. Geophys. Geosyst.*, *11*, Q10W07, doi:10.1029/2010GC003200.
Reyre, D. (1984), Remarques sur l'origine et l'évolution des bassins sédimentaires africains de la côte atlantique, *Bull. Soc. Geol. France*, *26*(6), 1041–1059.
Rowland, S. K., and H. Garbeil (2000), Slopes of oceanic basalt volcanoes, in *Remote Sensing of Active Volcanism*, *Geophys. Monogr. Ser.* vol 116, edited by P. J. Mouginis-Mark, J. A. Crisp, and J. H. Fink, pp. 223–247, AGU, Washington, D. C., doi:10.1029/GM116p0223.
Schellart, W. P. (2000), Shear test results for cohesion and friction coefficients for different granular materials: Scaling implications for their usage in analogue modelling, *Tectonophysics*, *324*, 1–16.
Schreurs, G., et al. (2006), Analogue benchmarks of shortening and extension experiments, in *Analogue and Numerical Modelling of Crustal-Scale Processes*, edited by S. J. H. Buiter and G. Schreurs, *Geol. Soc. London Spec. Publ.*, *253*, 1–27.
Suh, C. E., S. N. Ayonghe, and E. S. Njumbe (2001), Neo-tectonic earth movements related to the 1999 eruption of Cameroon Mountain, West Africa, *Episodes*, *24*(1), 9–12.
Suh, C. E., R. S. J. Sparks, J. G. Fitton, S. N. Ayonghe, C. Annen, R. Nana, and A. Luckman (2003), The 1999 and 2000 eruptions of Mount Cameroon: Eruption behaviour and petrochemistry of lava, *Bull. Volcanol.*, *65*, 267–281.
Suh, C. E., J. F. Luhr, and M. S. Njome (2008), Olivine-hosted glass inclusions from scoriae erupted in 1954–2000 at Mount Cameroon volcano, West Africa, *J. Volcanol. Geotherm. Res.*, *169*, 1–33.
Suh, C. E., S. A. Stansfield, R. S. J. Sparks, M. S. Njome, M. N. Wantim, and G. G. J. Ernst (2011), Morphology and structure of the 1999 lava flows at Mount Cameroon volcano (West Africa) and their bearing on the emplacement dynamics of volume-limited flows, *Geol. Mag.*, *148*(1), 22–34.
Thierry, P., L. Stieltjes, E. Kouokam, P. Ngueya, and P. M. Salley (2008), Multi-hazard risk mapping and assessment on an active volcano: The GRINP project at Mount Cameroon, *Nat. Hazards*, *45*, 429–456.
Tibaldi, A. (1995), Morphology of pyroclastic cones and tectonics, *J. Geophys. Res.*, *100*(B12), 24,521–24,535, doi:10.1029/95JB02250.
Tibaldi, A., F. L. Bonali, and C. Corazzato (2013), The diverging volcanic rift system, *Tectonophysics*, doi:10.1016/j.tecto.2013.1011.1023.
Ubangoh, R. U., B. Ateba, S. N. Ayonghe, and G. E. Ekodeck (1997), Earthquake swarms of Mt Cameroon, West Africa, *J. Afr. Earth Sci.*, *24*(4), 413–424.
Ubangoh, R. U., I. G. Pacca, and J. B. Nyobe (1998), Palaeomagnetism of the continental sector of the Cameroon Volcanic Line,West Africa, *Geophys. J. Int.*, *135*, 362–374.
Walter, T. (2003), Buttressing and fractional spreading of Tenerife, an experimental approach on the formation of rift zones, *Geophys. Res. Lett.*, *30*(6), 1296, doi:10.1029/2002GL016610.
Walter, T. R., and F. Amelung (2003), Surface deformation observed by INSAR during the 1999 and 2000 eruptions on Mount Cameroon, West Africa, paper presented at EGS - AGU - EUG Joint Assembly, Nice, 6-11 April.
Walter, T. R., A. Klugel, and S. Munn (2006), Gravitational spreading and formation of new rift zones on overlapping volcanoes, *Terra Nova*, *18*(1), 26–33.
Wandji, P., J. P. F. Tsafack, J. M. Bardintzeff, D. G. Nkouathio, A. K. Dongmo, H. Bellon, and H. Guillou (2009), Xenoliths of dunites, wehrlites and clinopyroxenites in the basanites from Batoke volcanic cone (Mount Cameroon, Central Africa): Petrogenetic implications, *Miner. Petrol.*, *96*(1–2), 81–98.
Wantim, M. N., C. E. Suh, G. G. J. Ernst, M. Kervyn, and P. Jacobs (2011), Characteristics of the 2000 fissure eruption and lava flow fields at Mount Cameroon volcano, West Africa: A combined field mapping and remote sensing approach, *Geol. J.*, *46*(4), 344–363.
Wantim, M. N., M. Kervyn, G. G. J. Ernst, M. A. del Marmol, C. E. Suh, and P. Jacobs (2013), Numerical experiments on the dynamics of channelised lava flows at Mount Cameroon volcano with the FLOWGO thermo-rheological model, *J. Volcanol. Geotherm. Res.*, *253*, 35–53.
White, D. J., W. A. Take, and M. D. Bolton (2001), Measuring soil deformation in geotechnical models using digital images and PIV analysis, in *10th International Conference on Computer Methods and Advances in Geomechanics*, Tucson, Ariz.
Zogning, A. (1988), LeMont Cameroun, un volcan actif: Contribution à l'étude de géographie physique appliquée, PhD thesis, 447 pp., Université de Yaoundé.